Erasmus Mundus Joint Master Degree in Nuclear Physics

The influence of rhenium addition on radiation damage and deuterium retention in tungsten

Master's Thesis

Alan Ricardo Cintora de la Cruz

Supervisors: Dr. Mikhail Zibrov, Dr. Eleonora Viezzer.

Universidad de Sevilla

Max Planck Institute for Plasma Physics

Abstract

In recent decades, tungsten (W) has proven to be a promising material that could be used to manufacture components in the vessel of a fusion reactor, such as the walls or the divertor. Radiation defects produced by the 14 MeV neutrons created in DT fusion reactions in this plasma-facing material (PFM) must be studied to evaluate its potential. Additionally, Rhenium (Re) presence in W-based plasma-facing components (PFC), produced as a transmutation element created by the same irradiation, must be as well considered.

To evaluate the Re influence on the displacement damage creation in this PFM, W single-crystal samples with different Re concentrations (0, 1, 3 and 6 at.%) were irradiated with 20 MeV W^{6+} ions in a Tandem accelerator up to 0.5 displacements per atom (dpa) at the damage peak, considering three different conditions 1) Irradiation at room temperature (T = 295 K), 2) Irradiation at high temperature (T = 1350 K) and 3) Irradiation at room temperature followed by annealing at high temperature. Subsequently, the three sets of samples were exposed to D plasma in an ECR source at a sample temperature of 370 K for 72h. Finally, to calculate the total D retained by the samples after the plasma exposure, which indicates the levels of the defect concentration after the irradiation, two experimental techniques were applied: Nuclear Reaction Analysis (NRA) and Thermal Desorption Spectroscopy (TDS).

From this systematic comparison, three general results were obtained. First, Re presence seems to reduce the trapped D concentration for the samples conditioned (irradiated or annealed) at high temperature, reaching differences up to almost two orders of magnitude between the pure W sample and the W-Re alloy with the highest Re fraction. Second, the conditioning temperature reduces the concentration levels of radiation defects in the samples, reaching differences up to two orders of magnitude comparing room and high temperature conditioning. Finally, irradiation and annealing at high temperature showed differences among themselves; even though both showed the same behavior, the Re influence differed by up to 1 order of magnitude, being irradiation at high temperature the treatment that reduced the D retention the most.

These general observations were acquired independently through both experimental meth-

ods. Furthermore, the obtained results agree with previous studies regarding the Re presence in W. This thesis, however, presented a more systematic approach to compare some of the parameters analyzed in precedent works. More of this methodical investigation can be applied to further assess the plasma-compatibility of W as a PFM, considering more parameters or circumstances that will be present in a fusion reactor environment.

Acknowledgements

The work presented in this thesis would not have been possible without the help and support of many people, to whom I am deeply grateful. First, I would like to thank my supervisor Mikhail Zibrov, who guided me throughout the whole development of this project, patiently providing me with the necessary knowledge and tools. I would like to thank Wolfgang Jacob and Thomas Schwarz-Selinger for granting me the opportunity of developing this thesis at the Max Planck Institute for Plasma Physics, and for providing me with guidance concerning the development of my scientific career. I would like to express my gratitude to the rest of my colleagues at the E2M division for the scientific discussions that enlightened this work and for the constant willingness to help. Special thanks to Thomas Dürbeck for aiding me with the operation of TESS, to Martin Balden and Katja Hunger for the support with the SEM and EDX studies, and to Joachim Dorner and Michael Fußender for operating the Tandem accelerator.

I wish to thank my supervisor at the University of Seville, Eleonora Viezzer, who during the master's also provided me with knowledge in plasma physics that deeply strengthened my interest and passion for fusion technology.

I am thankful to the Erasmus Master's in Nuclear Physics programme that granted me the opportunity to greatly boost my scientific career during the last two years, allowing me not only to study at top-level institutions like the University of Seville, the University of Padova or the University of Caen, but also to perform research work in centers like CERN, INFN Legnaro, GANIL and IPP. I am deeply grateful to all the professors and administrative staff that make this master's degree possible. Special thanks to Pepe Arias and José Antonio Lay who, in my view, act beyond duty for the sake of the programme.

I would like to thank all the people that encouraged me to go forward throughout the entirety of this master's. I am keenly thankful to the wonderful friends I met both in Sevilla and Munich, as well as to my Mexican friends who have always supported me from the distance. Thank you Ali for being the biggest inspiration and reason to keep going for the past two years. Finally, thanks to all my family, without whose undying faith, support, motivation and love I would not have made it this far. This milestone also belongs to you. Gracias Salvador, Lupita y Güero. Gracias totales.

List of Acronyms

at.fr.	Atomic fraction
DEMO	Demonstration Fusion Power Plant
dpa	Displacements per atom
EDX	Energy Dispersive X-Ray
ITER	International Thermonuclear Experimental Reactor
NRA	Nuclear Reaction Analysis
PFC	Plasma-Facing Component
PFM	Plasma-Facing Material
PKA	Primary Knock-on Atom
QMS	Quadrupole Mass Spectrometer
SEM	Scanning Electron Microscopy
TDS	Thermal Desorption Spectroscopy
TESS	Thermal Effusion Spectroscopy Setup
UHV	Ultra-High Vacuum

Contents

Chapter 1

Introduction

Nuclear fusion has been depicted for over 60 years as a possible source of energy with many potential applications. With the increasing climate crisis over the last decades, fusion power has been as well portrayed as a clean and safe option to satisfy humanity's long-term energy needs, given the minimal production of greenhouse gases and radioactive waste, the inherent safety of the reaction process, and other advantages that this technology represents in comparison with other well-known energy sources. Particularly, the fusion reactions involving hydrogen isotopes, deuterium (D) and tritium (T), are nowadays the main candidates to produce power in a controlled environment, due to the relatively easy access to them as fuels (specially D, which exists naturally as one part of ~ 6000 in water) and their energy release [1, 2]. The main reactions involving these isotopes are as follows:

$$\begin{aligned} \mathrm{D} + \mathrm{T} &\rightarrow^{4} \mathrm{He} + \mathrm{n} + 17.6\mathrm{MeV} \\ \mathrm{D} + \mathrm{D} &\rightarrow^{3} \mathrm{He} + \mathrm{n} + 3.2\mathrm{MeV} \\ \mathrm{D} + \mathrm{D} &\rightarrow \mathrm{T} + \mathrm{p} + 4.0\mathrm{MeV} \end{aligned} \tag{1.1}$$

Magnetic confinement is currently one of the main approaches to achieve a sustainable reaction cycle in a controlled environment. The development of this technology has reached the crucial full feasibility demonstration phase, with the International Thermonuclear Experimental Reactor (ITER) on the verge of initiating operations during the next few years. ITER is the world's largest fusion device and it is designed to be the core base for the future demonstration (DEMO) reactor, intended to be the first fusion power plant. Several institutes and entities across the world have studied the experimental conditions and implications to reach magnetic confinement and realized that the interaction of the edge-plasma with the plasma-facing components (PFCs) plays a key role that determines the performance of fusion reactors [3].

In an ITER-like device, PFCs are expected to withstand fluxes in the range of $10^{19} - 10^{24}$

particles/(m^2s) of hydrogen isotopes and impurities (e.g. helium, nitrogen) with energies varying from several eV to several keV and steady heat fluxes reaching up to several MW/m^2 [4, 5]. Additionally, these components will be subjected to high fluxes of energetic neutrons, which result as a product of the reactions shown in Eq. 1.1. These neutrons, that reach energies up to 14 MeV, will introduce radiation defects in the plasma-facing materials (PFMs) and cause transmutations (i.e. the conversion of one chemical element into another) resulting in activation of the material and retention of fuel and reaction products in the bulk [6]. Given that the reactor's wall must endure these conditions with little or no maintenance during extended periods of operation (several months or even years), a suitable selection of the PFMs must be broadly investigated considering all the aforementioned circumstances.

During the last three decades, high-Z materials have been investigated as potential candidates for PFMs. Tungsten (W), in particular, has already been selected as the main option for many PFCs due to its advantages in comparison with other materials in operation conditions. While these advantages are mainly related to its high temperature-handling capability, making tungsten already a suitable candidate, it must be also taken into account that this material might face problems of other kind, such as the plasma compatibility and radiological issues [7].

Due to the constant neutron flux to which the PFCs are subjected, it is expected that radiation defects will be created in the PFMs, gradually altering its lattice structure and, in consequence, its performance. Furthermore, these neutrons are expected to create the already mentioned transmutations. In the case of tungsten, simulations have already shown that, for a DEMO-like device, rhenium (Re) will be present as the main transmutation element, with a concentration of $\sim$ 4 at.% (atomic percentage) after five years of operation [8].

Several studies have been carried out to investigate W as a PFM along with the influence of its transmutation elements. One of the main approaches is to manufacture W and W-Re alloy samples and expose them to irradiation conditions comparable to those found in a fusion environment. Due to the lack of a reliable fusion-like neutron source, heavy ions have been utilized as a surrogate technique. In these studies, the degrading level of the samples have been characterized according to the deuterium retained after exposure to this hydrogen isotope, which is also related to the evolution of the defects caused by the irradiation. Several variables have been proven to have a significant influence on the PFMs performance, e.g. the rhenium concentration, the damage levels, the irradiation temperature [9, 10, 11]. Although these studies are well in agreement with each other, a systematic comparison of the considered variables is still to be carried out.

Throughout this master thesis, the line of research open by the recently mentioned studies

is further investigated. W alloys with concentrations ranging from 0 to 6 at.%Re were irradiated with heavy ions considering two different scenarios: room temperature damaging, widely studied in the antecedent works, and high temperature damaging, as a more accurate representation of the conditions to which PFCs will be exposed. Subsequently, the damaged samples were exposed to deuterium plasma. The deuterium retention was then analyzed through two experimental techniques: Nuclear Reaction Analysis (NRA) and Thermal Desorption Spectroscopy (TDS). The objective of this work is to provide a clearer view of W as PFM, focusing on the transmutation effect that will naturally arise in reactor conditions and taking into account simultaneously some of the variables that have been previously proven important for the experiments of this kind.

All the experimental work was carried out at the facilities of the Max-Planck Institute for Plasma Physics (IPP), located in Garching, Germany. The analysis tools and technical aid were as well provided by the "Plasma Edge and Wall" (E2M) division at the IPP.

Chapter 2

State of the Art

2.1 Hydrogen implantation in metals

In fusion devices, the hydrogen isotopes interacting with the walls are found mostly in atomic, rather than molecular, form. It is thus important to study the difference between the interactions of metals with hydrogen in molecular and atomic form. Furthermore, the understanding of the atomic interactions with metals is necessary to predict the recycling of hydrogen on the walls, the hydrogen inventory within the first wall and, as it is of interest for this work, the permeation of hydrogen through the wall [12].

To describe the interaction of hydrogen, both in molecular and atomic form, with the metal surfaces, Lennard-Jones first proposed the idealised potential energy diagram shown in Fig. 2.1 [14]. In this scheme, the potential energy of a single molecular H atom, i.e. $\frac{1}{2}H_2$, is taken as zero at infinity, which in consequence, sets the potential energy of one atomic H atom at half the dissociation energy of the H_2 molecule (2.25 eV).

In the region near the surface, approaching from infinity, adsorption of hydrogen might take place. This, however, differs for the molecular and atomic form. The adsorption of molecular hydrogen is called physisorption, while the adsorption of molecular hydrogen is called chemisorption. Physisorption takes place when molecular hydrogen acquires an activation energy E_p and finds its site in a shallow potential well, characterized by the heat of physisorption Q_p. With enough energy, the molecular hydrogen reaches then the dissociation point (much lower than the disociation energy in vacuum), where the molecular and atomic curves intercept and which is also the chemisorption activation energy E_c. The atomic hydrogen finds then its place at the potential well determined by the heat of chemisorption Q_c. It is noticeable that $Q_c > Q_p$ and that the adsorbed atom is significantly closer than the molecule due to chemical interaction.

Once the H atoms are chemisorbed by the metal surfaces, they can penetrate into the

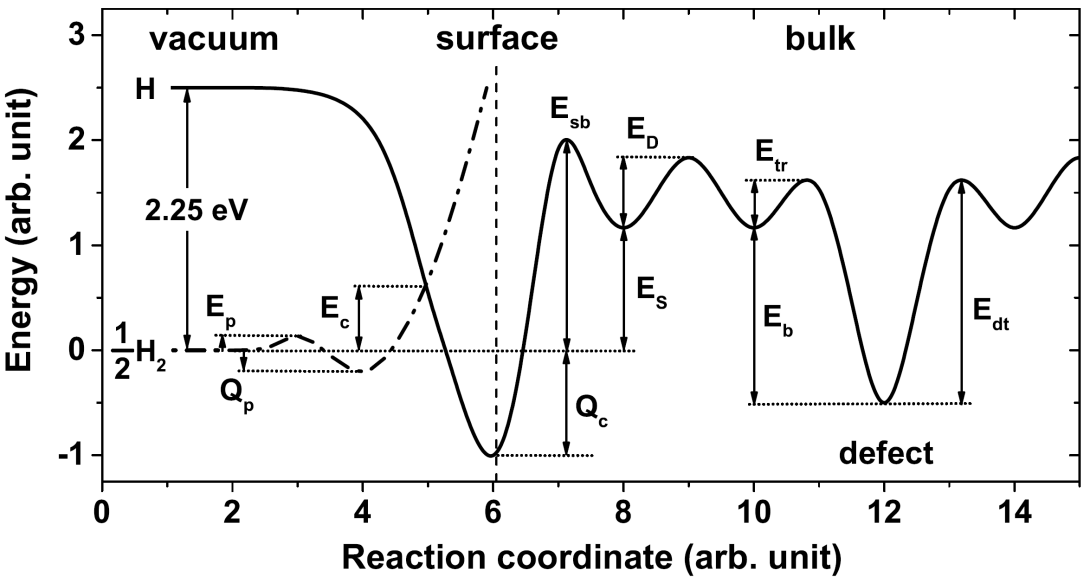

Figure 2.1: Potential energy scheme for atomic and molecular hydrogen around the surface of a metal. E_p and E_c are the activation energies for physisorption and chemisorption, respectively, while Q_p and Q_c are the heats of physisorption and chemisorption, respectively. E_{Diff} is the diffusion activation energy, E_S is the heat of hydrogen solution and E_{sb} is the absorption activation energy. To characterize defects, E_{tr} is the trapping activation energy, E_b is the defect binding energy and E_{dt} is the detrapping energy [13].

bulk. This penetration, called absorption, requires an additional energy E_{sb}, larger than the heat of hydrogen solution E_S (i.e. the energy of the atom in the bulk relative to the molecular H_2 gas). These atoms can either diffuse deeper into the metal or go back to the chemisorbed state, possibly recombine into an H_2 molecule in the physisorbed state and finally reach again the gas state.

The model described above is relevant for the case of molecular hydrogen. Energetic hydrogen atoms or ions impinging on a metal surface may be either reflected after one or several collisions with the target atoms or they may be slowed down to thermal velocities within the first layers of the material. This latter process, called implantation, takes place when the hydrogen atoms or ions impinge with energies above E_{sb} (typically above few eV), thus penetrating into the metal by bypassing the chemisorption state. This process results typically in hydrogen concentration levels that greatly exceeds those corresponding to uptake from the gas state [15].

The absorbed or implanted hydrogen atoms occupy the interstitial sites of the metal lattice, i.e. the empty space between the atoms forming the crystal structure. This interstitial sites can be as well represented by an energy potential well defined by the diffusion activation energy E_{Diff}. If the atoms occupying an interstitial site gain energy above E_{Diff}, the diffusion process takes place, as the atoms are able to jump between adjacent interstitial positions. Fick's Law describes the diffusive flux $\vec{J}$ [atoms/(m^{2}s)] as:

$$\vec{J}(\vec{r},t) = -D\nabla C(\vec{r},t) \tag{2.1}$$

where $C(\vec{r},t)$ stands for the local concentration of the hydrogen and D is the diffusion coefficient, which depends on the diffusion activation energy E_{Diff} and the temperature T in the form:

$$D = D_0 \exp\left(-\frac{E_D}{k_B T}\right) \tag{2.2}$$

where k_B is the Boltzmann constant. To picture a more complete description of the hydrogen transport in metals, it is possible to determine the evolution of the concentration profile, also known as the diffusion equation, following the continuity equation:

$$\frac{\partial C(\vec{r},t)}{\partial t} = -\nabla \vec{J}(\vec{r},t) + S(\vec{r},t) \tag{2.3}$$

where $S(\vec{r},t)$ represents the density of volumetric hydrogen sources. Eq. 2.3 is also known as Fick's second law [12, 13].

2.2 Lattice defects in metals and their interaction with hydrogen

In fusion reactors like ITER and DEMO, the surfaces of the PFCs are exposed not only to high heat but also to high particle flux. In particular for the DT reaction shown in Eq. 1.1, 14.1 MeV neutrons are expected as a reaction product, reaching fluxes of $\sim 10^{18}(\text{m}^{-2}\text{s}^{-1})$. Due to the energetic nature of these neutrons, radiation defects can be created not only in the near surface region but also through the entire PFC bulk. It becomes thus relevant to understand how these defects, along with other type of defects, can affect the performance of the fusion reactors [6].

In Sec 2.1, the description of the metals, along with its interaction with the hydrogen isotopes, was provided considering them as perfect crystal lattices. This however differs from the reality, where the PFCs are commonly manufactured with so-called intrinsic defects, such as dislocations, impurities, etc. Along with these defects, the already mentioned radiation damage must be considered when evaluating the performance of the PFCs.

The aforementioned description can also be extended to the case of imperfect bulks, i.e. metals containing lattice defects. These defects can be modelled as trapping sites, using the potential energy shown in Fig. 2.1, with different characteristics from those corre-

sponding to the regular interstitial sites. The defects are characterized by the activation energy for trapping an atom located inside the bulk E_{tr}, the defect binding energy E_b and the detrapping energy $E_{dt} = E_{tr} + E_b$ needed for the atom to escape the defect.

A radiation damage event may be defined as the redistribution of target atoms in a solid after the energy transfer from an incident projectile. This event is constituted by several processes occurring consecutively: first, the incident particle interacts with a lattice atom by transferring kinetic energy to the same atom, which is then known as the primary knock-on atom (PKA). This interaction displaces the PKA from its original lattice site and, given the sufficient energy, the passage of the PKA through the lattice can create additional knock-on atoms. Along with the secondary knock-on atoms, the PKA might be able to create a displacement cascade, to finally come to rest at an interstitial site [16].

The result of all these processes is a collection of various types of defects. The most basic type of radiation defect are the Frenkel pairs, defined as a pair of vacancy and interstitial atom, and these defects can accumulate to create clusters in the crystal lattice, that can as well migrate to produce additional clustering and dissolution of the clusters. Fig. 2.2 depicts some of the defects produced both intrinsically and through irradiation in the metal lattices of the PFCs

One of the most used parameters to determine the damage created in a solid due to irradi-

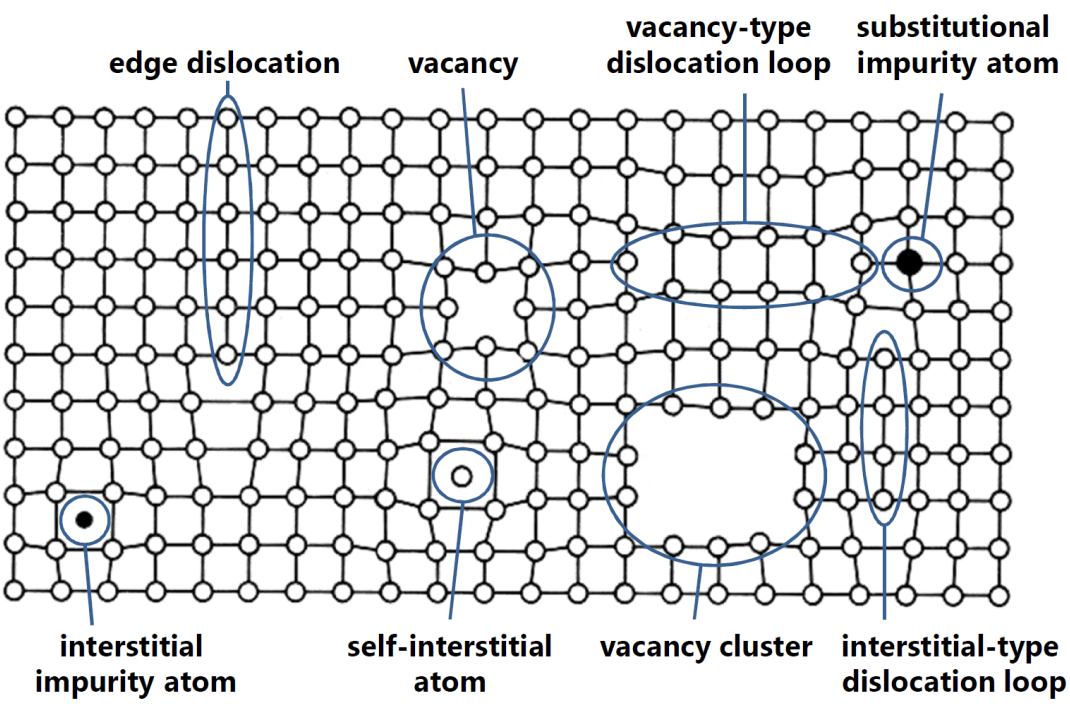

Figure 2.2: Several type of lattice defects produced intrinsically and by irradiation in a metal [13]. In the presence of hydrogen, each defect act as a trapping site for the H-atoms with a characteristic detrapping energy E_{dt} depending on the type of defect.

ation is the "displacement per atom" (dpa), which quantifies the number of displacements from a lattice site per lattice atom. This magnitude considers information about the material response, as well as the impinging particles flux and it is a measure of the damaged produce by the incoming particles, through the number of displaced atoms, rather than a quantification of the lattice defects created [17].

The commonly accepted method (NRT-dpa) to calculate the dpa describes the number of displacements ν_{NRT} as a function of the PKA energy E_{PKA}, according to:

$$\nu_{\mathrm{NRT}}(E_{\mathrm{PKA}}) = \begin{cases} 0 & E_{dam} < E_d \\ 1 & E_d \leq E_{dam} < 2E_d/0.8 \\ 0.8E_{dam}/(2E_d) & E_{dam} \geq 2E_d/0.8 \end{cases} \tag{2.4}$$

where E_{Diff} is the displacement threshold and E_{dam} is defined as E_{PKA} accounting for the inelastic energy loss according to the partitioning theory of Lindhard [18]. In irradiation damaging experiments, a common approach to estimate the damage created in the specimens is the calculation of the depth distribution, i.e. dpa as a function of penetration depth [13]. This parameter is described as:

$$\mathrm{dpa}(x) = \frac{N_{displ}(x)\Phi}{\rho} \tag{2.5}$$

where Φ is the incident fluence, ρ is the atomic density of the irradiated material and $N_{displ}(x)$ is the number of displacements per incident ion per unit depth. This last parameter is calculater through the SRIM code version 2013 [19], which performs Monte Carlo simulations of the displacement cascades generated by incoming projectile particles. In these simulations, the ν_{NRT} are calculated, following Eq. 2.4, to then obtain the $N_{displ}(x)$ function.

2.3 Tungsten as plasma facing material

PFMs for future fusion reactors like ITER or DEMO must be able to endure extreme environmental conditions such as high particle fluxes (neutron, hydrogen, helium), transient heat loads up to several MJ/m^2, and a steady state power fluxes up to 20 MW/m^2 [20, 21]. Thus, the desing of the PFCs for these devices has become highly dependent on the properties and characteristics of the PFMs.

During the last decades, several studies have shown that tungsten has large advantages over most candidates considered as potential PFMs. Among the most important features,

there are: high melting point, low erosion (i.e. high energy threshold for sputtering), high thermal stress resistance, high termal conductivity, low swelling, etc. Despite the disadvantages that it possesses (such as recrystalization, high Z and poor machinability), tungsten is the most promising material for the inner wall of future reactors. In consequence, it has already been selected as the PFM for a large part of the ITER divertor, during its initial phase and is planed to be fully used for this PFC in future stages.

It is, however, necessary to consider all the drawbacks that W as PFM represents, and further investigate its properties, behavior and evolution in fusion conditions by carrying out studies of several kind. Among the most important, there are the mechanical tests, thermal shock loading, thermal fatigue loading, He- and H-irraditation, and, as it is the interest of this work, neutron irradiation [7, 22].

2.4 Rhenium addition to tungsten and irradiation temperature influence

Since W might be used not only in PFCs like the divertor, whose lifetime is around 2 years, but also in parts of the fusion device that might last at least 5 years, the irradiation-induced embrittlement of this PFM has become a serious issue to address. Furthermore, it has become a case of study the tungsten evolution when exposed to a continuous fusion environment for prolonged periods.

One of the most notorious phenomena observed in simulations addressing this situation are the so-called transmutations, i.e. the change of the original atoms into neighboring elements. This effect is produced due to nuclear reactions occurring between the PFM and the radiation produced by the plasma. It has been observed that the main contribution to this phenomenon is induced by the 14.1 MeV neutrons that naturally arise from the main DT reaction [8].

Through these simulations, the transmutation of tungsten during the first years of operation of a DEMO-like power plant has been analyzed. Fig. 2.3 shows the evolution of concentration in at.%, i.e. the percentage of atoms of a given element in the material, during the first five years of operation, from an initially pure W-PFC.

It can be noticed that the main contribution from the transmutation elements comes from rhenium, reaching levels up to 3.80 at.% after the first five years of operation. It becomes thus relevant to study the influence of Re in W as a PFM, as it is the main objective of this work.

In recent years, Re addition to W has been studied in the framework of fusion technology,

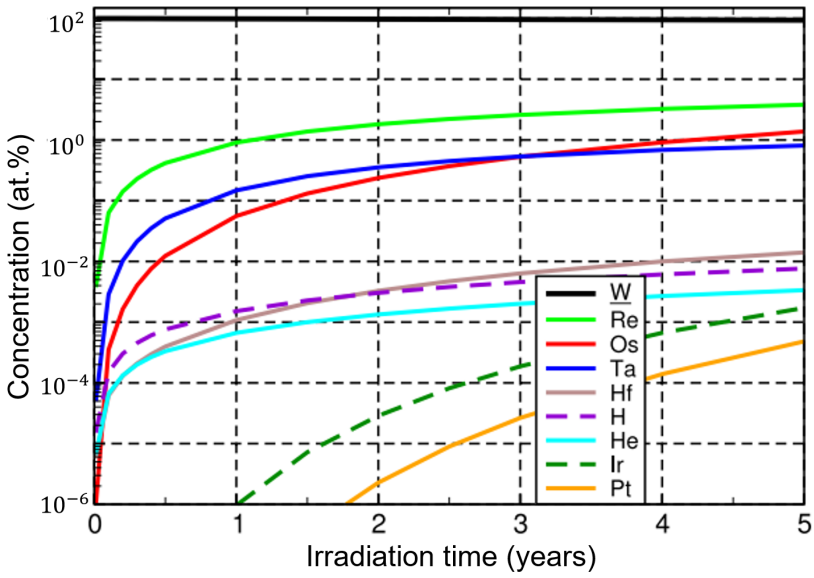

Figure 2.3: Simulation of transmutations evolution during the first five years of operation of a fusion power plant, from an initially pure W-PFC. The main contribution comes from rhenium (Re) which, after five years of operation reaches, levels up to 3.8 at.% [8].

focusing on the effects that arise from the neutron irradiation. Since a convenient source of fusion neutrons has not been available during these studies, the typical approach is to simulate the damage due to neutron irradiation, by making use of energetic heavy ions irradiation. It has been proven that, for the case of W-based materials, irradiation by MeV-range W ions has been found as the best proxy for neutron irradiation [9].

It is relevant for fusion devices to avoid absorption of plasma fuel elements such as D or T, for purposes of efficiency and safety. Hence, one of the most used probes to evaluate the PFCs' intergrity is the D retention after exposing these materials to this hydrogen isotope. Since the radiation-induced defects act as trap for D, it is expected to observe higher concentrations in irradiated materials [23]. Novel works have taken the approach of studying polycristalline samples of W-Re alloys, studying different experimental conditions to further comprehend the behavior of W as a PFM in fusion environmental conditions.

A study carried out by J. Wang *et al.* performed a comparison between different Re concentration levels in the W-Re alloy. Samples with 0, 1, 3 and 5 at.% of Re were analyzed after irradiation of 6.4 MeV Fe ions at 1073 K and after exposure of D_2 gas at 673 K. For comparison, another set of samples that were not irradiated was also analyzed after the D exposure stage [11]. As shown in Fig. 2.4, this study suggested that there might exist an effect from the different Re concentration levels in the sample, however, for this case, this difference is not shown to be significant, given the small differences. Furthermore, it is observed as well a reduction of D concentration levels for the non-irradiated set of samples, which would agree with the model suggesting that the radiation-induced defects

act as a trap for the D atoms that are absorbed into the lattice of the PFC.

The rhenium concentration in the samples, however, has not been the only parameter considered when performing these studies. The temperature at which the sample is exposed during irradiation (T_{irr}), has been also observed to change the D concentration levels in the samples.

Another study carried out by Y. Hatano *et al.* observed the influence of this irradiation temperature T_{irr} in samples of both pure W and W-5 at.%Re. This was performed by irradiating the samples with 6.4 MeV iron (Fe) ions and then exposing the irradiated samples to D_2 gas at 673 K [10]. In Fig. 2.5 are shown the D concentration levels for several values of T_{irr} at a peak damage level of 0.5 dpa. These results describe a clear inverse relationship between the D concentration in the samples and T_{irr}, particularly for the case of the W-Re sample.

Furthermore, from this study, it is also noticeable that post-irradiation annealing i.e. thermal treating at an elevated temperature (further details at Sec. 3.1.1) might as well influence the D retention levels, and, even more, it might not be comparable to irradiation at the same temperature as the annealing temperature T_{anneal}. This result possibly glimpses a reduction of concentrations of vacancy-type defects that behaves different when there is only high T_{irr}, rather than low-temperature irradiation followed by annealing at

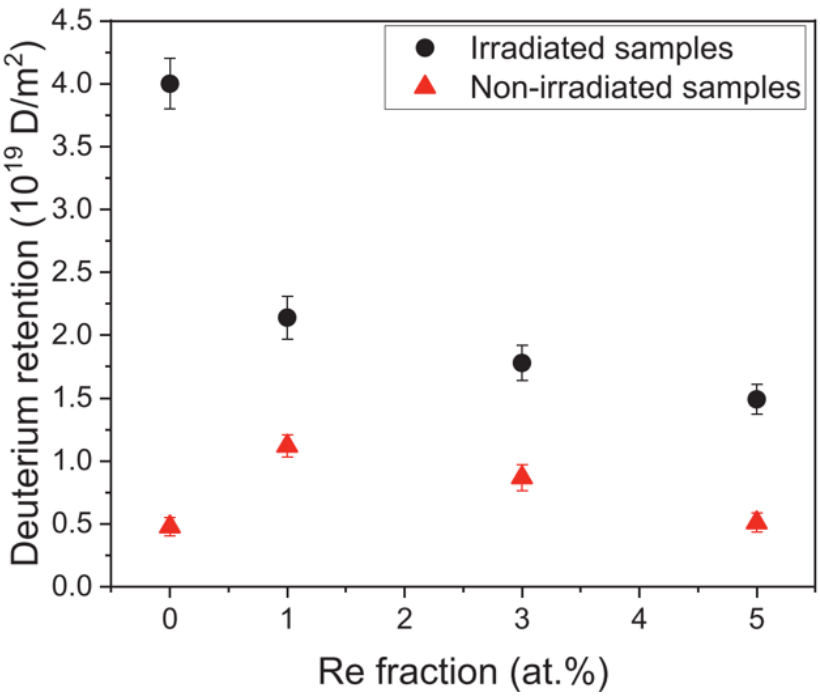

Figure 2.4: Study by J. Wang *et al.*, showing D concentration levels after D_2 exposure at $T = 673$K for varying Re concentration levels in sets of non-irradiated and irradiated samples. The damaging was produced by 6.4 MeV Fe ions at $T_{\text{irr}} = 1073$ K to a peak damage level of 0.5 dpa [11]. The results suggest a influence in the D concentration due to the presence of Re in the samples.

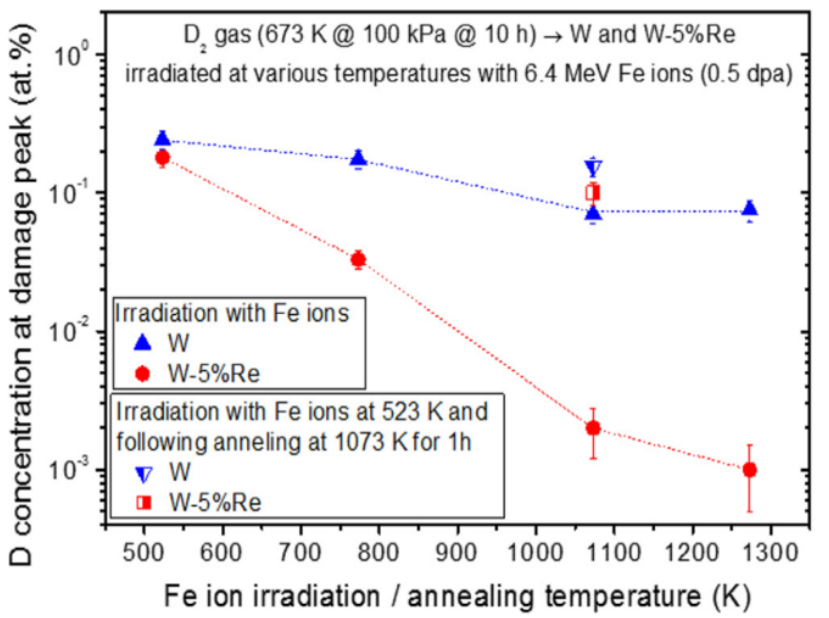

Y. Hatano *et al*, Nuclear Materials and Energy, 9 (2016) 93-97

Figure 2.5: Study by Y. Hatano *et al.*, showing D concentration levels after D_2 exposure at $T = 673$K of samples of pure W and W-5 at.%Re. for varying irradiation temperature T_{irr} of Fe ions. The irradiation was produced to peak damage level of 0.5 dpa. Results for samples irradated at $T_{\text{irr}} = 523$K and consecutively annealed at $T_{\text{anneal}} = 1073$ K for 1h are also shown [10]. The study indicates an inverse relationship between the irradiation temperature and the D concentration.

high temperature.

Through studies as the mentioned above, it has been shown that the Re addition to W-based PFCs is a key factor when optimizing the performance of a fusion device. Furthermore, it has been proven that several factors might play a significant role in these circumstances. Up until now there has not been a study that systematically compares some of these features of interests. Hence, this work is focused in studying the Re influence in W-Re alloys by controlling simultaneously both the Re concentration levels in the samples and the temperature at which the irradiation damage is produced. Similarly a comparison between irradiation at high temperature and irradiation at low temperature followed by annealing at high temperature is carried out.

Chapter 3

Experimental procedure

3.1 Sample preparation

To carry out the desired experiments for this project, several samples with different rhenium concentrations were considered. As shown in previous studies [10, 11, 23], the Re concentration region of interest lies between 0 and 6 at.%. Hence, in this work samples of pure W and W-Re alloys with concentrations of 1, 3 and 6 at.% were used to perform the systemic comparison.

To ensure a better comparison without effects of micro-structure, other than the Re concentration, the samples used during the experiments were single crystals, in contrast with most of the studies performed, in which polycrystalline samples were used. Even though this type of sample does not represent the real case for a W-based PFC, it might enlighten the desired observations in a clearer fashion.

The samples were manufactured by the Luch Research Institute/Research and Production Association (Federal State Unitary Enterprise, Podolsk, Moscow oblast, Russia), according to a preparation procedure that can be described in three general stages [24]:

1. Tungsten powder dried in vacuum is taken as starting material, from which rods are produced by hydrostatic compression to be consecutively dried, degased and sintered at high temperatures.

2. 2 mm grooves were cut on the surface of the rod along its axis. Then 2 mm diameter Re wires, whose preset weight determines the at.% concentration in the sample, were placed in the grooves. The rods are then melted in an electron-beam zone melting system to produce polycristalline rods.

3. The previously obtained rods were melted once again to obtain monocrystalline

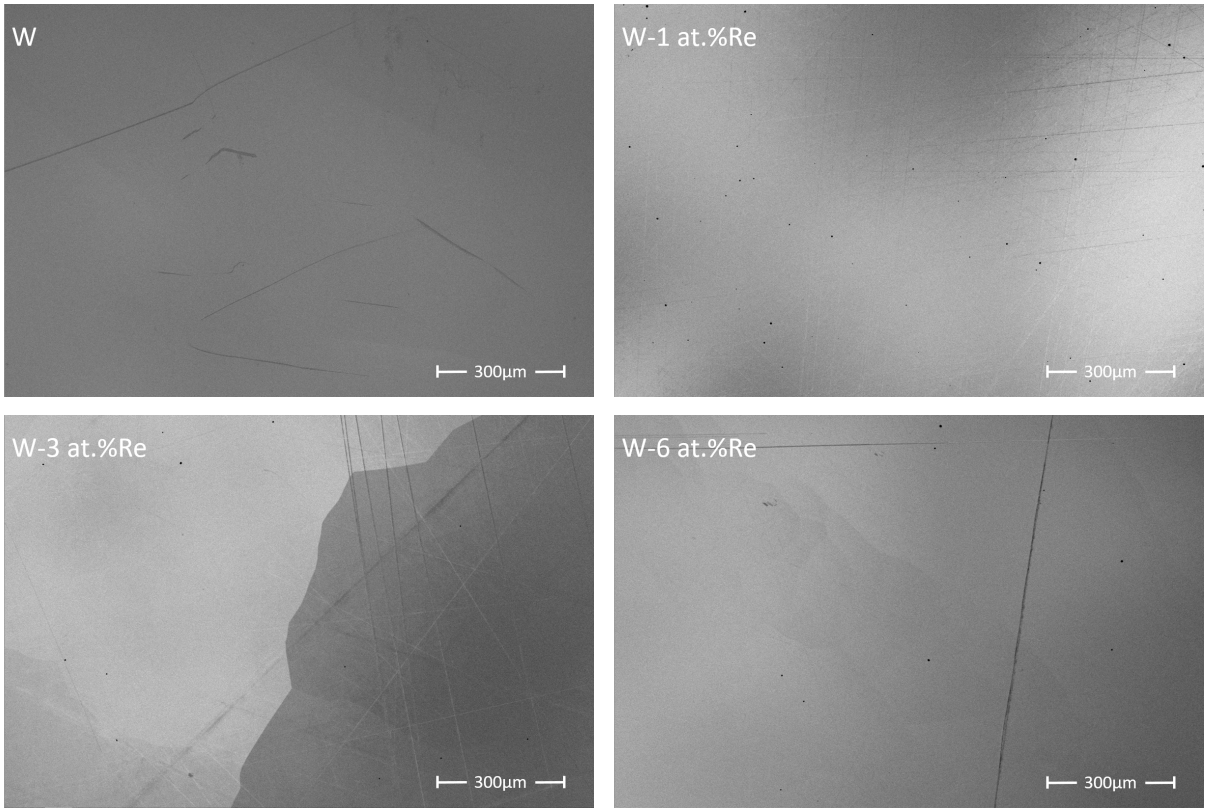

Figure 3.1: SEM images taken for a sample of each Rhenium concentration. Morphology defects such as scratches from imperfect polishing and pores can be observed for all the samples. For a given case, two lattice orientations can be observed, suggesting that some samples might not be entirely perfect single crystals. Cases like this present a characteristic grain size of few hundred μm

rods.

From the obtained material, single-crystal samples with 10×10 mm^2 surface and 0.7mm thickness and $\langle 111 \rangle$ orientation were manufactured. Before any treatment, all the samples were mechanically polished according to the procedure described in [25], until reaching a mirror-like finish. Then, they were cleaned in ultrasonic bath with isopropanol, acetone and high-purity acetone for 15 minutes, to finally be annealed as described in Sec. 3.1.1.

Surface morphology studies were performed on one sample for each Re concentration, as an example of the general characteristics of all the considered samples, with the aid of a scanning electron microscope (SEM) FEI HELIOS NanoLab600. SEM images were captured to characterize morphology defects that might have to be taken into account when assessing the results of this study. Fig. 3.1 shows a series of SEM images with the same magnification for a single-crystal sample of each W-Re alloy considered in this study.

From these SEM images, it is possible to identify several imperfections in the surface of the alloys. Plastic distortions formed as scratches arise from an imperfect polishing

treatment are present in most of the samples. Pores of similar size ($\sim 2-3\mu$m) are as well present in the near-surface region for every sample, all of them with comparable surface densities. Finally, for the observed W-3 at.%Re sample, different lattice orientations are present, suggesting that some samples might not be perfect single crystals. This was as well observed for some other samples and in all cases the characteristic grain size is a few hundred μm. Although this microscopy studies were not performed for every sample considered in this work, these roughly described characteristics might provide part of the explanation of the obtained results and must be considered both for possible inconsistencies and for the final conclusion.

In addition to SEM imaging, Energy Dispersive X-Ray (EDX) analysis was performed to determine the composition of the samples and assess the Re concentrations guaranteed by the manufacturer. This analysis, which can be found in Appendix A, resulted inconclusive due to the presence of contamination elements (e.g. C, O, Ni) located mainly in the samples' surfaces. Hence, this study relies on the Re fraction guaranteed by the manufacturer in every of the utilized samples.

To examine systematically all the considered effects a total of 3 sets of 4 samples (one sample for each Re concentration), in addition to one reference set, were used for this study. The differences among these sets are briefly explained in Table 3.1 and the procedure to condition them as described is detailed in sections 3.1.1 and 3.1.2. Consecutively, all the samples, including the reference set, were loaded with deuterium as described in section 3.1.3.

Table 3.1: Description of the varying treatment for every set of samples used to study deuterium retention. Each set is composed by 4 single-crystal W samples with 0, 1, 3 and 6 at.% of Re concentration.

Label	Set Number	Damaging	Annealing (post-damaging)
Reference	1	No	No
Room Temperature	3	295 K	No
High Temperature	2	295 K	1350 K
	4	1350 K	No

3.1.1 Annealing

Annealing is a thermal treating in which the samples are exposed to an elevated temperature for an extended period and then steadily cooled down. This process has mainly the objective of relieving stress in the material, removing surface impurities (such as oxygen and carbon) and degassing, mainly to remove hydrogen from the sample bulk [26].

Previous to the sample damaging, an annealing process was performed a the Tandem facility for every set at about 2500K in 6 series of 30 s, for a total of 3 minutes and, consecutively annealed at 2000 K for 5 minutes. Finally the ramping down until room temperature was performed along several minutes. The temperature at which the samples are annealed was regulated making use of an optical pyrometer.

In the case of one of the set of samples damaged at room temperature, a second annealing treatment was performed as described in Sec. 3.1.2.

3.1.2 Radiation damage creation at Tandem accelerator

Following some of the results in former studies, presented in Section 2.4, W ions were selected to reproduce the damage produced by fast fusion neutrons in the W and W-Re samples. From these same studies, it is known that the irradiation temperature T_{irr} might play a role in the material's performance. For this reason, two set of samples were damaged at room temperature $T_{\mathrm{irr}} = 295$ K (one of them to be afterwards annealed at high temperature) and other at high temperature $T_{\mathrm{irr}} = 1350$ K.

Damage at high temperature was studied, considering that in an operating fusion reactor PFCs will be subjected to heat loads that will take the PFCs well above room temperatures. In the case of e.g. W-armored divertor targets, surface temperature in the range of $\sim 900 - 2600$ K are expected [3], hence an irradiation temperature within this values was selected. Even though room temperature is not representative for a PFC, its study is a good benchmark, since several works have been carried out for this condition.

Damaging was achieved with 20 MeV W^{6+} ions created at the accelerator facility at IPP. These ions are created with a cesium sputter source from a tungsten carbide target. The ion charge state and energies are achieved at the 3MV Tandem accelerator located after the ion source. Finally the sample irradiation is performed in the TOF beamline, as schematized in Fig. 3.2.

For the irradiation at room temperature, every sample is clamped to a water-cooled copper holder, placed at the ion implantaiton chamber, that makes use of molybdenum (Mo) masks, with an opening area of 8×8 mm^2, to fix several samples simultaneously as depicted in Fig 3.3a. For irradiation at high temperature, each sample is mounted individually on a resistive heater (Boralectric© HTR1001) and clamped with a rectangular Mo mask with a circular opening of 9 mm diameter. To measure and control the temperature at which the samples are heated, a type K thermocouple was inserted into a hole besides the heater and a second thermocouple of the same type was clamped between the mask and the sample, as depicted in Fig. 3.3b.

The impinging beam is typically delimited by a water-cooled circular aperture (12 mm in

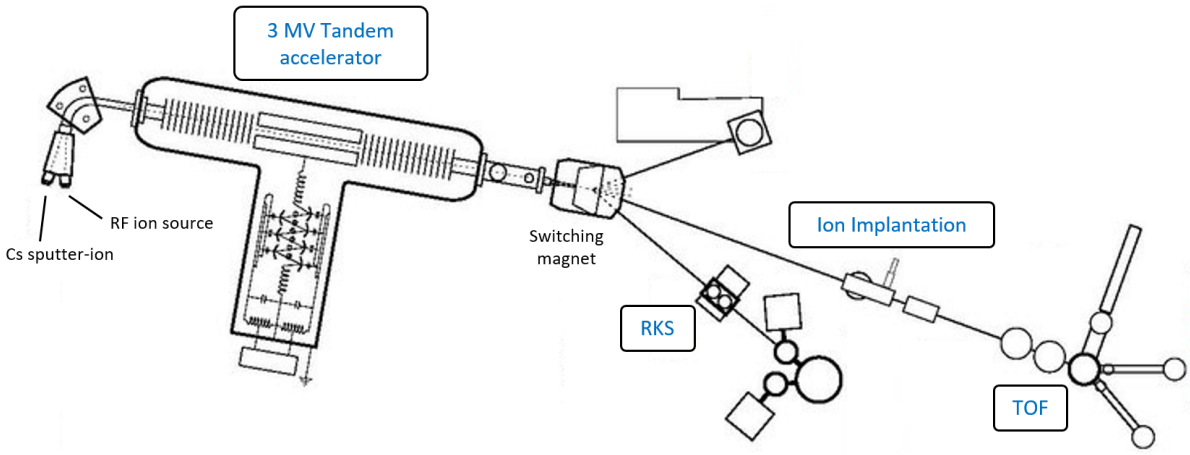

Figure 3.2: Scheme of the accelerator facility at IPP, featuring a 3 MV Tandem acclerator, two types of ion sources and several beamlines accessibles with the aid of a switching magnet. In the TOF beamline, the ion implantation chamber is located, where the damaging of the samples is performed. At another beamline the RKS set-up is placed, where the NRA measurements are carried out [27].

diameter) that is placed in front of the Cu sample holder, along with four Faraday cups, whose measured current is used to calculate the absolute tungsten flux [28], as shown in 3.3c. Usually, the W beam is focused onto the target with the aid of an electrostatic quadrupole triplet lens located at the exit of the Tandem accelerator. Then, the beam is scanned over an area up to 25×25 mm^2 to achieve an homogeneous implantation in the sample. This configuration was used for damaging at room temperature.

For damaging at high temperature, however, a defocused beam mode was selected, with the aid of the same quadrupoles. Several studies have shown that, even though defocusing might signify an important loss of the beam, this mode works better as a surrogate technique to replace neutron irradiation, in comparison with focused beam scanning. Due to the intermittent nature of beam scanning mode, which operates at a given frequency, defocusing shows a steadier swelling rate in the damaged material [28, 29, 30, 31].Despite this recommendation, scanning was also performed to the defocused beam, in order to ensure a better homogeneity and to facilitate later analysis.

Fig. 3.3d shows a photography of the W^{6+} defocused beam impinging on a piece of quartz, used to describe the particle distribution through the brightness of the material. The picture, taken after the damaging of one of the samples, shows an almost completely equally distributed beam, with slightly bigger fluxes, for instance, in the lower region of the quartz.

Using the SRIM 2013 software [19] and the W^{6+} ion flux measured by the Faraday cups, it is possible to calculate the primary displacements generated in the samples and, therefore, the damage depth distribution, as described in Sec. 2.2. This calculation is performed

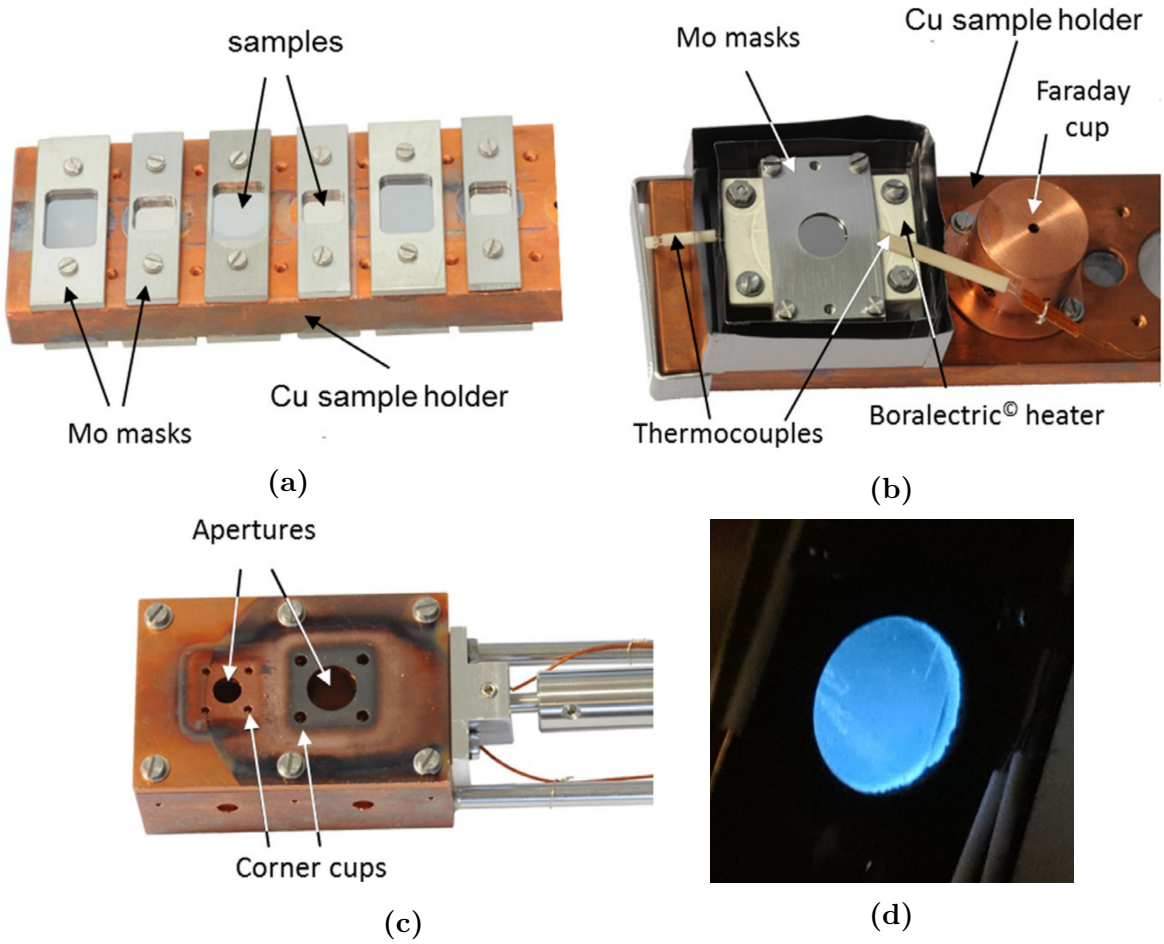

Figure 3.3: Set-up at the implantation chamber (a) Sample holder used to irradiate samples at room temperature; (b) Sample holder used to irradiate samples at high temperature, featuring the Boralectric© heating element and two thermocouples to measure the temperature; (c) Apertures and Faraday cups used to measure the W^{6+} flux [28]; (d) Defocused beam distribution impinging on a piece of quartz. Brighter areas represent a bigger particle flux.

considering a W atomic density of $\rho = 6.31 \times 10^{28}$ atoms/m^3, a displacement threshold $E_d = 90$ eV, a lattice binding energy of 0 eV and the "Quick Kinchin Phase" option, as recommended by precedent studies [32, 33]. For the irradiation of every sample, an absolute fluence of $\Phi = 1.7 \times 10^{18}$ W^{6+}/m^2 was pre-selected, resulting in a 2.4 μm damaged layer with 0.5 dpa at the damage peak.

The selection of the dpa level was made according to a previous study [34] that relates the D concentration at damage peak to the peak damage level in irradiated W samples, as shown in Fig. 3.4. In this plot, it can be observed that, for the case of irradiation at room temperature, the D reaches a saturation level for damage levels higher than 0.23 dpa. Thus, the 0.5 dpa value was selected considering its located well after the saturation point. This study is also taken as a reference to select the high irradiation temperature at $T_{\text{irr}} = 1350$ K.

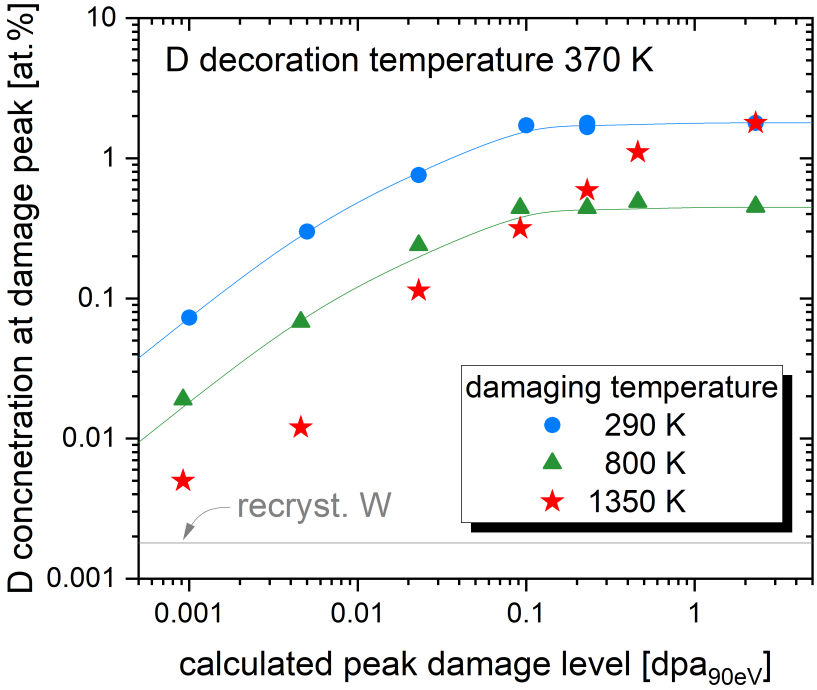

Figure 3.4: D concentration at damage peak as a function the peak damage level for pure W samples [34]. A saturation point is observed above 0.23 dpa in the case of damaging at room temperature

The processing of damaging was carried out maintaining a pressure below 10^{-5} Pa at the ion implantation chamber. In the case of the irradiation at high temperature, liquid nitrogen was constantly applied to the chamber to avoid the out-gassing from hydrocarbons, hence, prevent the impurity flux into the samples. This procedure was also performed to maintain the desired vacuum levels.

After the irradiation one set of samples damaged at room temperature was continuously annealed at 1350 K for a period equivalent to the average time duration of irradiation damage at high temperature, i.e. 6 h. This was performed to assess whether there is a difference between damaging at high temperature and damaging at room temperature followed by annealing at high temperature. In contrast with the first annealing, this second treatment was carried out using the same set-up where high temperature damage took place.

3.1.3 Deuterium plasma exposure at PlaQ

The deuterium loading into the three damaged set of samples, along with the reference set, was carried out by exposure to a low-flux plasma. The setup PlaQ is an Electron-Cyclotron-Resonance plasma source that features a biased sample holder and whose magnetic field B is generated by a single magnetic coil. The microwaves are created by a

magnetron with $f = 2.45$ GHz and $P_{\max} = 200$ W, and, with the aid of a waveguide ending in a aluminium oxide window, they are coupled from the vacuum vessel from the high B field. The ECR plasma is then confined to a cylindrical mesh cage with 14 cm of diameter and 15 cm of height and whose bottom is composed by a steel plate with circular aperture. Through this aperture, the plasma is able to freely expand and reach the sample holder. PlaQ also features a movable Langmuir probe, designed to measure the ion flux profile, and an IR camera to track the internal temperature at the sample holder when performing the plasma exposing procedure [35, 36]. The configuration of PlaQ is schematized in Fig. 3.5.

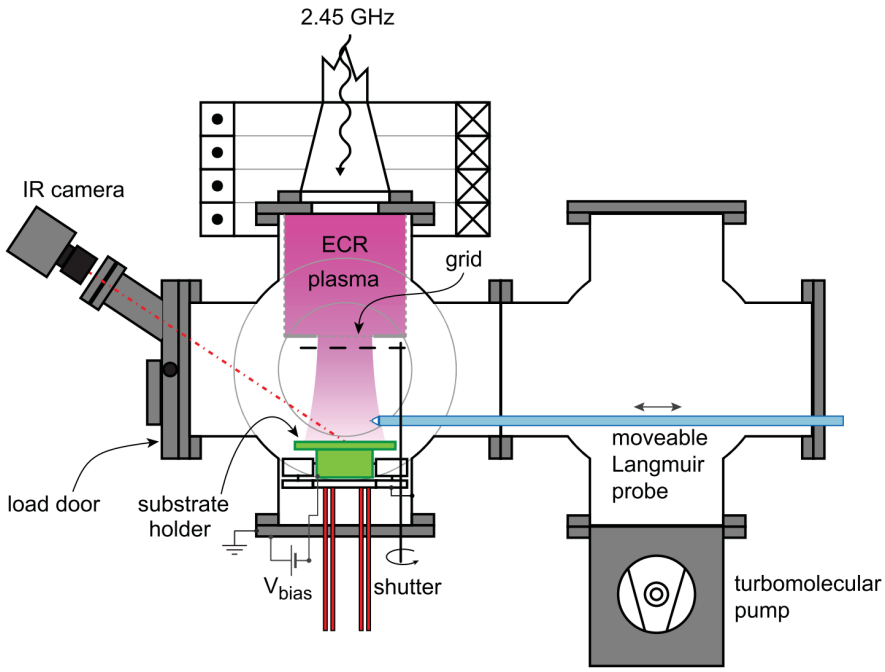

Figure 3.5: Schematic respresentation of the ECR plasma source PlaQ [36].

In the case of D plasma, PlaQ is capable of delivering a total flux of $\sim 10^{20}$ D(m^{2}s)$^{-1}$, in the form of 94% D_3^+, 3% D_2^+ and 3% D^+. The energy of the ions impinging on the sample can be adjusted by tuning the negative bias V_{bias} of the sample holder [36].

The sample holder allows multiple samples to be exposed to the plasma. Once the samples are mounted and prior to the exposure, the vacuum chamber is pumped overnight until a pressure in the order of 10^{-6} Pa is reached. Then, the ECR plasma is ignited and blocked using a metal shutter located under the ECR cage to prevent the exposure in the burn-in phase of the plasma. During this phase, the discharge is operated for 1h until stable plasma conditions are reached and the surface of the cage is cleaned of adsorbed impurities from the plasma-wetted surfaces.

The four sets of samples were exposed to the plasma beam for a total of 72h at 370 K, using a bias of $V_{bias} = -20$ V, which results in a mean energy per deuterium $E_D \approx 10$ eV/D. This energy value is considerably below the threshold for creating displacement

damage or sputtering and it prevents the formation of a near-surface deuterium-rich layer [37].

3.2 Analysis techniques

3.2.1 Nuclear Reaction Analysis

Nuclear Reaction Analysis is a non-destructive technique that makes use of the radiation emitted instantaneously from a projectile-nucleus interaction to detect the presence of an element in a sample. Typically, this method consists in the bombardment of light ions whose energies are in the range of MeV. Given the cross-section of the reaction, it is possible to determine the concentration profile through the measurement of the energy spectra of the reaction products [38].

For deuterium depth profiling, the NRA technique is commonly applied using the D(^{3}He,p)α reaction, which has a Q-value, i.e. energy release of 18.4 MeV, resulting in proton energies in the range of 11-14 MeV. This characteristics allows an easy filtering of backscattered primary particles by making use of stopper foils [40]. Fig. 3.6 shows the differential cross-section $d\sigma_{\mathrm{NRA}}/d\Omega$ of the reaction at a laboratory angle of $\theta_{\mathrm{LAB}} = 135°$ (relevant for the experimental set-up used), which has a maximum at about 690 keV [39].

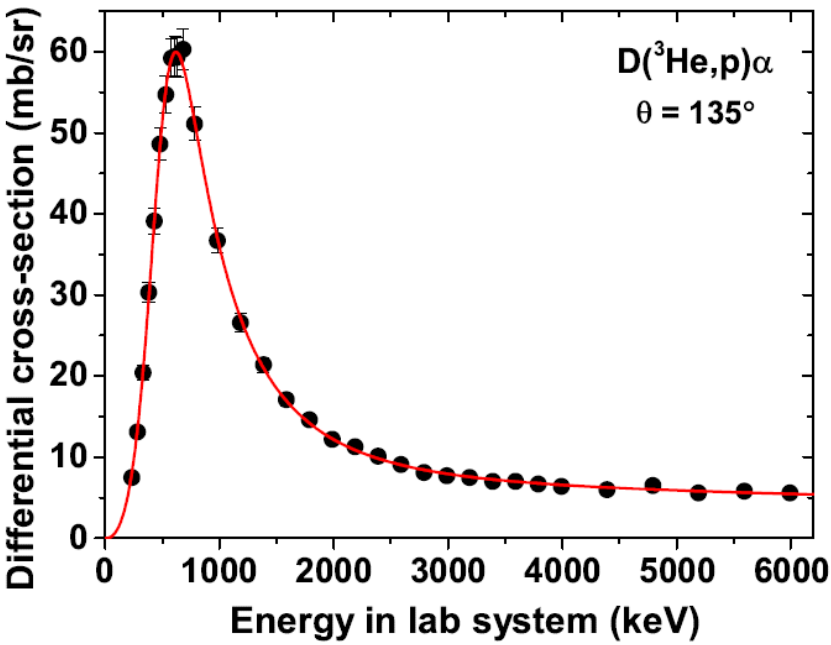

Figure 3.6: Data points for the differential cross-section of the D(^{3}He,p)α reaction at $\theta_{\mathrm{LAB}} = 135°$. The red solid line corresponds to the fit used by SIMNRA with a specific function used for optimization described in [39].

The results provided through this technique using one single incident energy don't provide all necessary information to reconstruct the depth profile, hence, several ^{3}He energies are considered to carry out the NRA. In this particular study, eight different different incident energies were used: 0.50, 0.69, 0.80, 1.20, 1.80, 2.40, 3.20 and 4.50 MeV. Fig. 3.7 shows the simulated effective differential cross-section $d\sigma_{NRA}/d\Omega \times \eta_{beam}$,which takes into account the stopping profile of the ^{3}He beam impinging on a tungsten specimen, as a function of the penetration depth for some of the selected energies [41].

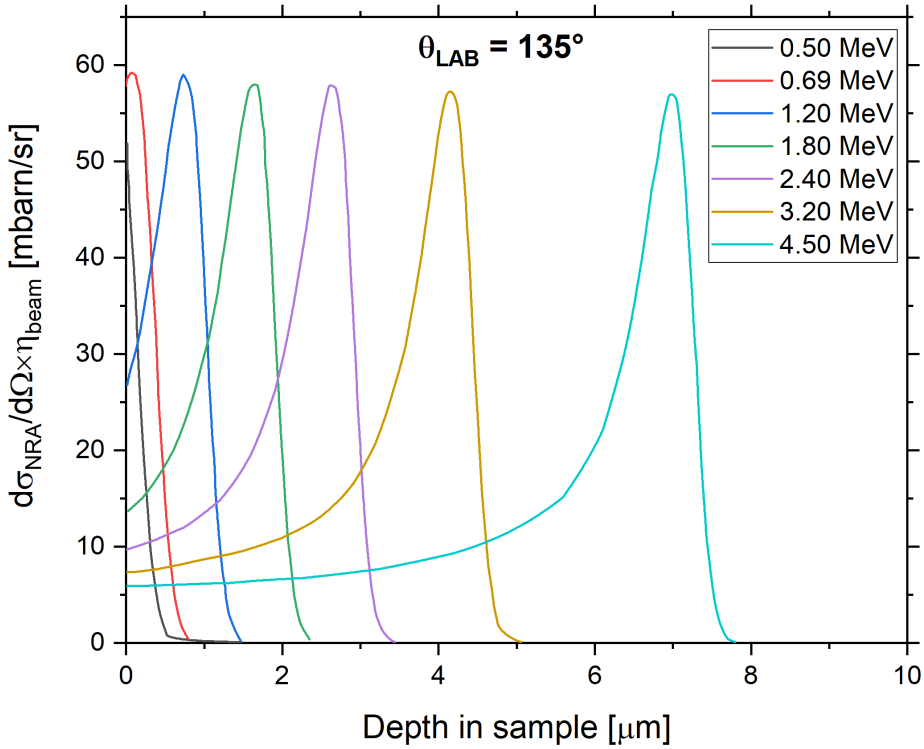

Figure 3.7: Effective differential cross-section $d\sigma_{NRA}/d\Omega \times \eta_{beam}$ of the D(^{3}He,p)α reaction versus penetration depth in a tungsten specimen at $\theta_{LAB} = 135°$. The factor η_{beam} accounts for stopping profile of the ^{3}He beam impinging on a tungsten specimen.

Along with the energy spectra provided by the proton yields of the reaction, the α energy spectra at low energies (up to 0.80 MeV) may complement the primary information, since they provide better depth resolution in the near-surface region. The accumulated charge of ^{3}He ions was set in the range of 10-40 μC, depending on the differential cross-section levels, to achieve a reasonable statistical significance, i.e. a minimal detectable D concentration in the order of 10^{-6} at.frac.

To perform these measurements, the accelerator facility features another beamline, which can be accessed through a switching magnet located after the tandem accelerator, containing the RKS scattering chamber, depicted as well in Fig. 3.2. This multi-purpose chamber is designed to perform NRA, as well as other techniques, and is equipped with a retractable sample holder that allows the user to select one of the up to 8 samples

mounted for the analysis. All the measurements are performed by targeting the beam at the center of the selected sample. Along the chamber's inner surface, several detectors are distributed, as shown in Fig. 3.8. For the experiments performed the next detectors were used:

- Back scattering counter (*RKS102*) at 102°, used for the α particles detection with a solid angle of $\Omega = 7.65$ msr
- Large proton counter (*ProL*) at 135°, equipped with a thick stopper foil for filtering backscattered ^{3}He, so that only high-energy protons are detected. It is designed with a large solid angle, $\Omega = 78.7$ msr
- Annular Proton Counter (*Ann*) at 165°, designed with ring shaped form with a better depth resolution for D depth profiling in exchange for a smaller solid angle, $\Omega = 19.5$ msr

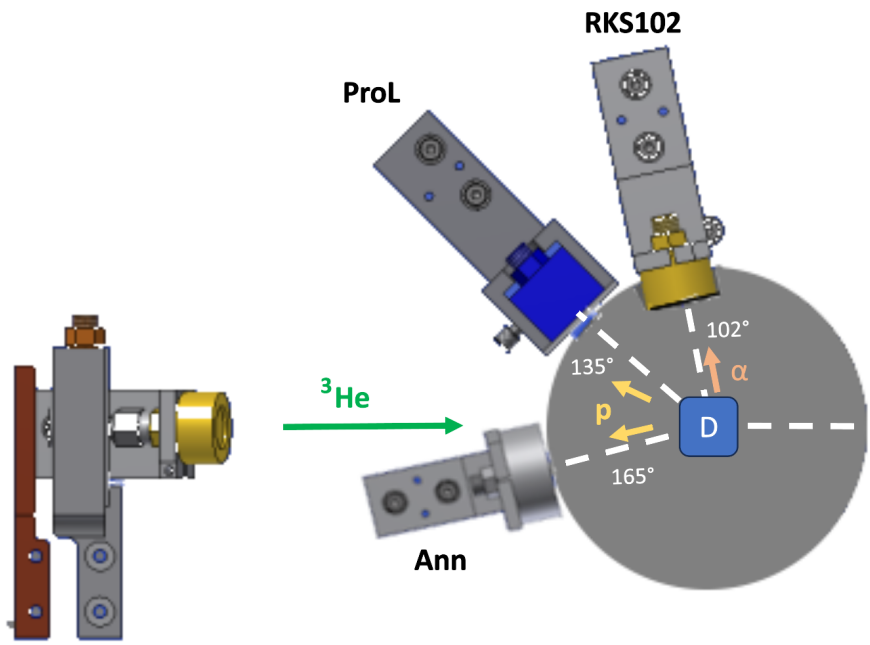

Figure 3.8: RKS multi-purpose scattering chamber designed to perform NRA studies.

The calibration of the detectors is carried out at every energy by taking the known peaks from the D(^{3}He,p)α reaction. This is accomplished with the aid of a 20nm thick amorphous deuterated hydrocarbon (a-C:D) layer on silicon. For each of the detectors, the same beam energies were used and the measured peaks were fitted with asymmetric Gaussian functions and, consecutively, related to the known proton energies for the reaction. This procedure was performed independently for every day of measurement to ensure a better

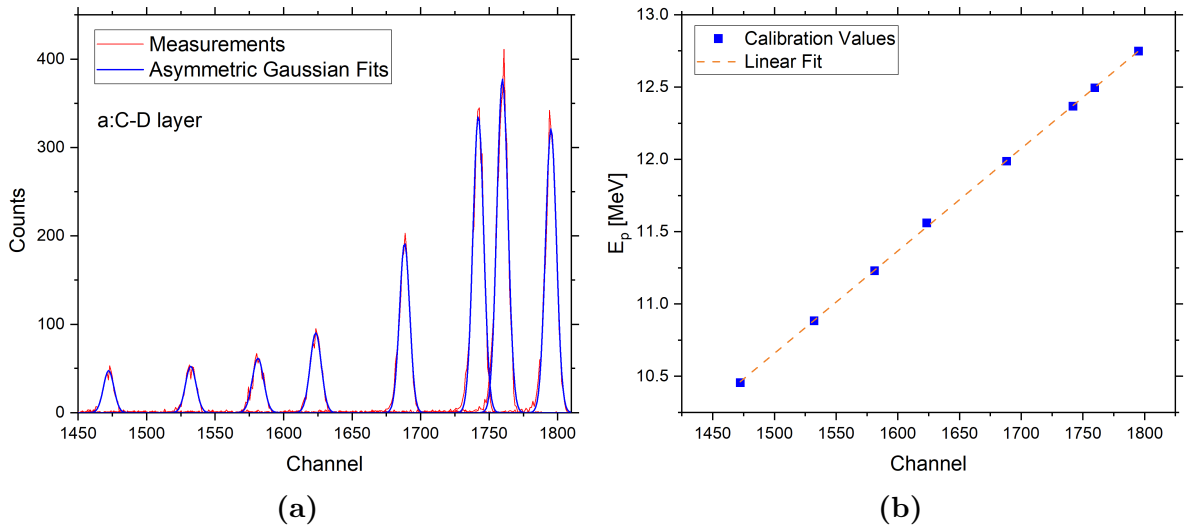

Figure 3.9: Calibration for *Ann* proton detector using an a-C:D layer, through the D(^{3}He,p)α reaction. (a) Measurements for every ^{3}He energy with their correspondent asymmetric Gaussian fit. (b) Linear fit relating the found peaks with the known proton energies of the reaction.

interpretation of the results. Fig. 3.9 shows a sample calibration for the *Ann* detector from the fitting of the measured peaks to the calibration with the known proton energies.

The measurements for every energy and for a given sample were analysed with a combination of the SIMNRA software [42], in charge of calculating the energy spectra, and the NRADC program [43], responsible for the deconvolution of the data resulting from the study of the reaction with energy variations of the incident beam. Taking into account the spatial overlapping of the effective differential cross-section shown in Fig. 3.7, NRADC is programmed to fit simultaneously all the recollected data in order to reconstruct the deuterium depth distributions, which are discretised into layers with constant deuterium concentration due to the limited resolution available. NRADC optimises the layers (number, thicknesses, concentrations) by using a Markov-Chain Monte Carlo method, resulting in the depth profile with the maximum likelihood and confidence intervals. To ensure a good result for every analysis, the agreement between the data and the simulations was set with $\chi^2/n < 1$, where n is the number of channels. Fig. 3.10 shows the case of the NRADC fit for the proton and alpha spectra measured for a given sample.

Finally, to assess how uniform the irradiation damage on the whole sample surface was, lateral scanning was performed. This technique consists in counting the reaction products (usually the protons) of the NRA reaction, at different points in the sample. Typically, due to the nature of the set-up, the ^{3}He beam is focused at relative positions to the center, moving in a single direction. The raw data obtained is enough to reveal any difference of D presence at different points, which would translate into inhomogenities of the irradiation damage.

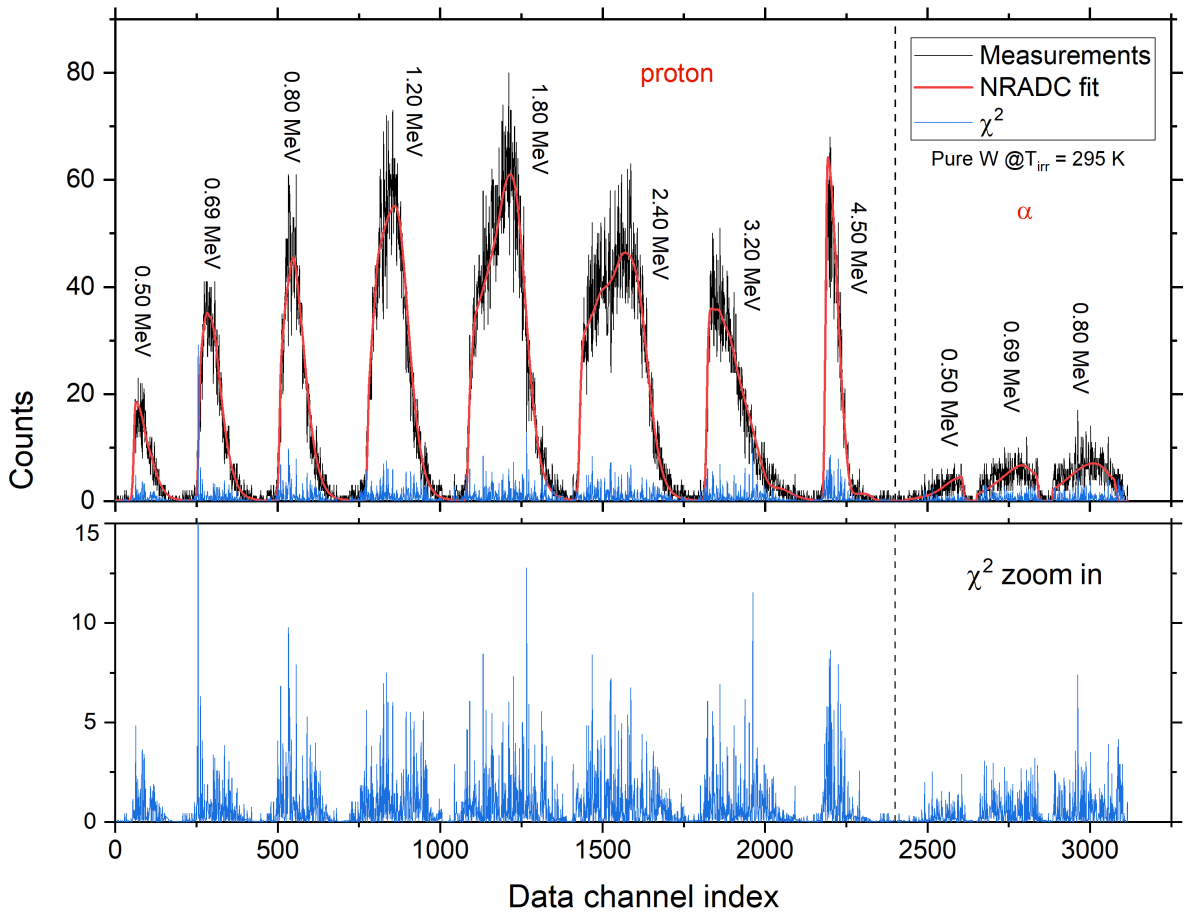

Figure 3.10: Data recollected for one sample (Pure W, $T_{\text{irr}} = 295$ K), along with the fit calculated by the program NRADC and the error χ^2. For this case, the simulation agrees with the measurements according to $\chi^2/n = 0.65$.

3.2.2 Thermal Desorption Spectroscopy

Thermal Desorption Spectroscopy (TDS) is a technique used to study the behaviour of gases in solids to retrieve information about their characteristics, such as the binding energy. This method consists in the heating of the sample in ultra-high vacuum (UHV). By increasing the temperature, the gaseous atoms receive sufficient energy from the lattice, which increases their probability to escape from their corresponding location sites. This release from the bulk site gives rise to the diffusion of the atoms within the lattice causing a repeated process of retrapping of the atoms in different bulk sites until they eventually reach the surface. Then, the atoms recombine into molecules to finally desorb from the solid into the vacuum. The sample is typically heated to such temperatures that guarantee a full release of the retained atoms, which, in their molecular form, are registered and distinguished through a mass-spectrometer. Due to the nature of this technique, it is considered to be a destructive method [44, 45].

To perform a TDS measurement, it is common to use linear heating ramps, which fa-

cilitates the analysis of the desorption spectra. Hence, the function that describes the temperature evolution with time is defined as $T(t) = T_0 + \beta t$, where T_0 is the initial sample temperature (typically room temperature) and $\beta = \mathrm{d}T/\mathrm{d}t$ is the heating rate.

The TDS measurements performed for this work were carried out at the thermal effusion spectroscopy setup (TESS) installation, whose layout is depicted in Fig. 3.11. TESS is an UHV experiment that features a turbomolecularpump, which provides high pumping speed, and a quadrupole mass spectrometer (QMS) [46]. Additionally TESS also features a quartz tube, where the samples to be studied can be loaded and then analyzed individually, and a retractable tube furnace that performs the sample heating until reaching the desired temperature, at which all the gaseous species are fully desorbed. A valve that separates the main chamber and the quartz tube is also present to ensure a correct pumping in the tube after the loading of the samples.

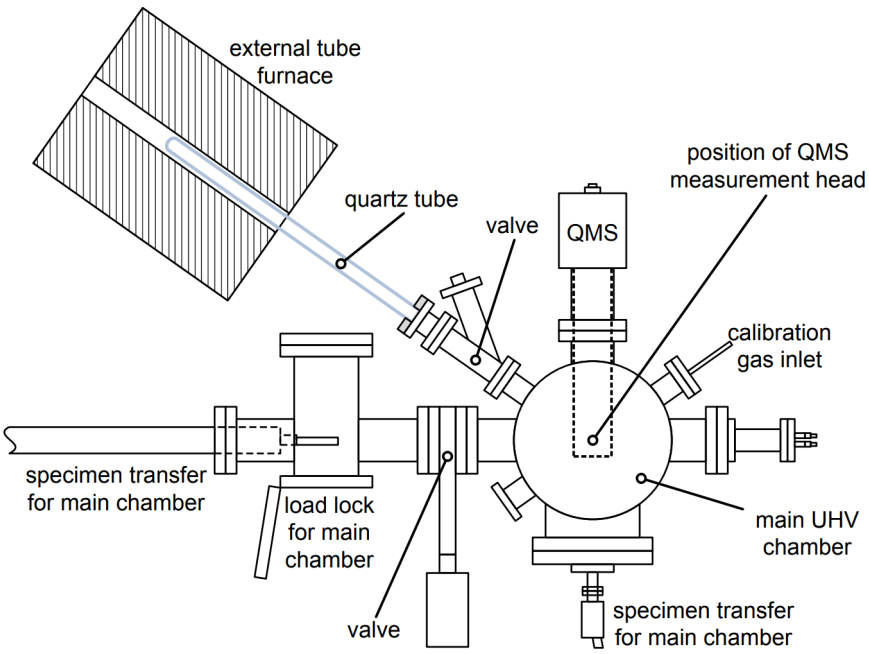

Figure 3.11: Scheme of the TESS set-up, used to perform TDS measurements [41].

The calibration for the QMS signal is carried out using a calibrated leak that is connected through a valve to the main chamber. The calibration was performed using a gaseous D_2 tank with known flow rate.

During TDS the oven was programmed for a heating rate of $\beta = 0.05$ K/s, starting at $T_0 = 295$ K, and the temperature was controlled making use of a sheathed thermocouple in contact with the sample. This slow heating rate was chosen due to the fact that, under these conditions, tungsten specimens' temperature increase is close to linear, making interpretation of TDS spectra easier [41]. It must be considered, however, that for the initial part of the temperature ramp, the heating of tungsten samples is not linear. Thus,

the sample temperature and the oven temperature must be calibrated in independent experiments making use of a K-type thermocouple welded to a tungsten sample. This calibration yields a polynomial fitting relating the readings of the oven's temperature to the actual sample temperature.

Similar to the NRA analysis explained previously, the aim of the TDS measurements is to detect the D atoms present in each of the considered samples. Due to this reason, it is relevant to take into account all the molecular contributions of deuterium in the QMS readings. Hence, not only the D_2 molecules (mass 4) are considered, but also HD, HDO and D_2O (mass 3, 19 and 20, respectively). These four spectra are considered in this analysis to account for the total D retained in the samples.

Finally, to get a more accurate representation of the spectra, a background measurement without any sample is performed to take into account residual background signals. These readings are set as the zero-line for each of the QMS readings considered in this analysis.

An example of TDS spectra is shown in Fig. 3.12, where the desorption flux is shown as a function of time for all the molecular contributions of deuterium that were considered. The sample temperature evolution shown corresponds both to the oven readings and to the polynomial calibration performed to those measurements. For the analysis of the spectra

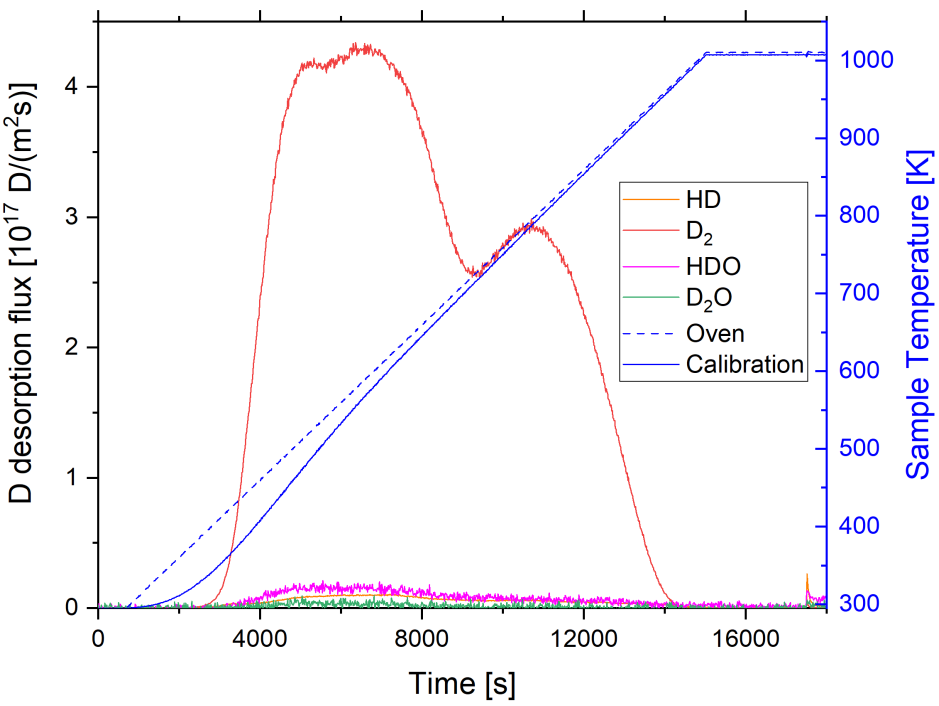

Figure 3.12: Example of TDS spectra as a function of time for the considered deuterium molecules (HD, D_2, HDO and D_2O) desorbed from a sample. The sample temperature is shown both from the oven readings, programmed with a heating rate of $\beta = 0.05$ K/s and an initial temperature of $T_0 = 295$ K, and after the polynomial calibration.

across the different type of samples only the D_2 readings are considered, given that they represent the major contribution among the four masses with a difference of at least one order of magnitude. The contributions of the four masses are, however, considered for the quantification of the total D retained in the samples.

Besides providing information about the total amount of D atoms retained in the analyzed samples, TDS spectra also provide information on the different type of defects introduced in the bulk. Given that the desorption of particles depends on the energy provided by heating the sample, several peaks might show in the spectra, which correspond to particles released from defects with different detrapping energies E_{dt} [47]. Even though this qualitative analysis alone does not provide direct information on the nature of those defects, which is out of the scope for this project, it offers a valuable parameter to compare the radiation damage created given the different Re concentrations and the different experimental conditions among the three main set of samples.

Chapter 4

Results and Discussion

The depth profiles for every set of sample were derived based on the NRA measurements with the aid of the NRADC program up to a depth of ∼7 μm. The results are presented as constant D concentration levels for the calculated layers, as explained in Sec. 3.2.1. For each layer, the concentration values are derived with an uncertainty in the positive and negative direction. These results are presented along with the damage profile produced by 20 MeV W^{6+} ions, which was calculated with SRIM up to 0.5 dpa at the damage peak for a W sample, neglecting the Re fraction. The calculations were performed mostly with the proton measurements captured by the *Ann* detector at the RKS chamber, except for samples with very poor statistics (usually layers with D concentrations lower than 0.01 at.frac.) for which the *ProL* detector was used.

The TDS spectra for every set of samples are presented, using the measurements from D atoms recombined into D_2 molecules. These spectra provide information on the total D retained in the samples, through the desorption flux as a function of sample temperature, and on the difference in radiation defects between the different analyzed samples, as described in the previous chapter.

4.1 Room Temperature Samples

Fig. 4.1 shows the D depth profiles corresponding to the set of samples irradiated at room temperature $T_{\mathrm{irr}} = 295$ K. In the region surrounding the damage peak, D retention does not present a significantly different behavior between the alloys with different Rhenium fraction, given that the four samples present concentrations with ratios no larger than 1.2 at the damage peak. At higher depths (beyond 2 μm) there seems to be higher D penetration for some samples, being pure W the sample presenting larger concentrations in the deep layers of the material. Despite the shallow differences, there might exist a

correlation between the Re fraction in the sample and the total D concentration, since the values around the damage peak seem to progressively increase from the pure W sample up until the W-6 at.%Re sample. Whether this correlation is significant must be assessed using a chosen parameter, such as the average concentration around the damage peak (details in Sec. 4.3).

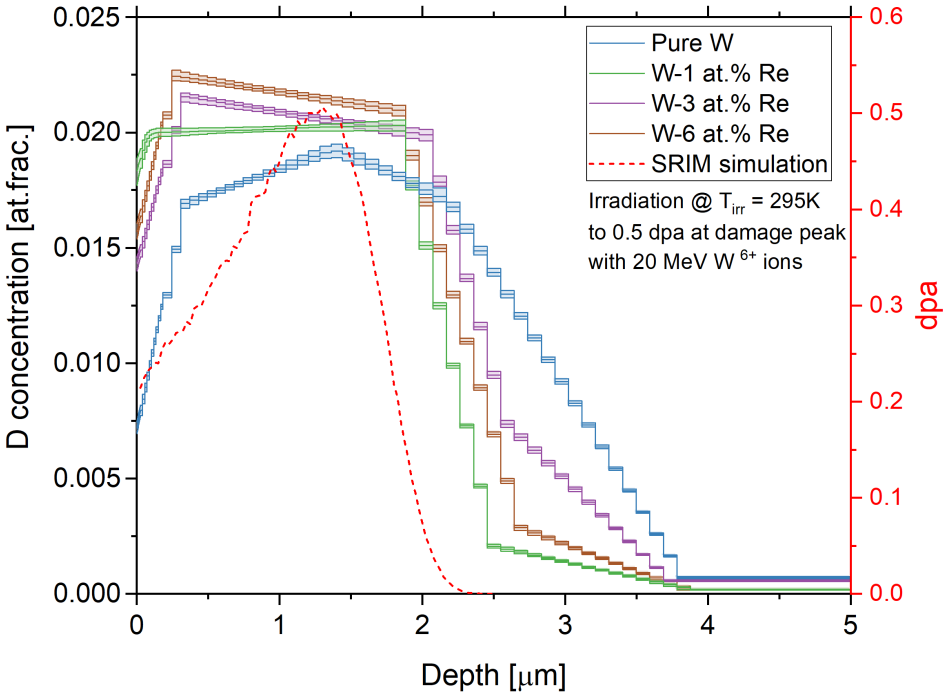

Figure 4.1: D Depth profiles derived from NRA measurements for the set of samples irradiated at room temperature $T_{\text{irr}} = 295$ K. SRIM calculations for the damage produced in a W sample by 20 Mev W^{6+} ions are overlayed.

The TDS spectra for the same set of samples are shown in Fig. 4.2. It can be observed that, although with different intensities, the four samples present spectra with similar characteristics, i.e. two desorption peaks, one of them being broad at $\sim$ 550 K and the second being narrower at $\sim$ 800 K. These two peaks sharing characteristics among the different samples suggest that the radiation defects trapping the D in the samples are similar despite the different Re concentrations in the alloys. Furthermore, it can as well be noticed that the largest ratio of desorption rate at any of the peaks is no larger than 1.3.

Higher D retention seem to be observed for higher Re fraction in the samples, as observed with NRA, except for the pure W sample. It is again unclear whether this correlation is significant for the samples irradiated at room temperature.

From both NRA and TDS analyses, it is not lucid if there is a significant effect arising from the Re fraction variation in the samples, given than the type radiation defects appear to be similar for all the samples and that the D concentration, both from the depth profiles and

the desorption fluxes, remain in the same order of magnitude. It is however, relevant to consider the possible direct correlation between D retention and Re fraction, suggesting that rhenium, for samples irradiated at room temperature might slightly enhance the defect creations and hence result demerital for W as PFM.

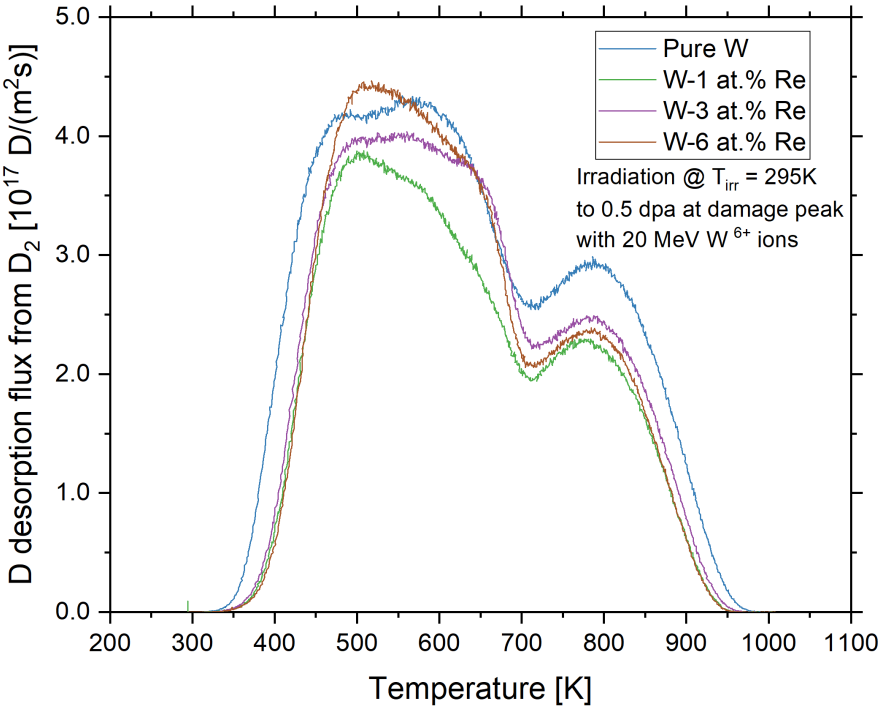

Figure 4.2: TDS spectra for the set of samples irradiated at room temperature $T_{\text{irr}} = 295$ K, showing the D release rate of D_2 (Mass 4) molecules.

4.2 High Temperature Samples

As it was already described in Sec. 3.1, two different sets of samples were considered for the "High Temperature" condition: 1) Samples irradiated at high temperature ($T = 1350$ K) and 2) samples irradiated at room temperature ($T = 295$ K) and consecutively annealed at the same high temperature during 6h, interval similar to the irradiation time at high temperature. The main purpose is to check if there is a difference between these two treatments at high temperature, in correspondence with the Re influence evaluation.

Fig. 4.3 shows the D depth profiles for the set of samples irradiated at $T_{\text{irr}} = 1350$ K. The results of this analysis show clear differences in the D concentration in the region surrounding the damage peak, between the different Re fractions. It can be observed that the biggest difference at the damage peak of is of almost 2 orders of magnitude. For the deeper layers (beyond 2 μm) of the sample, the pure W sample presents higher D concentration, hence deeper penetration (up to 3.5 μm into the material), in comparison

with the W-Re alloys at any Re fraction.

In the case of the W-1 at.%Re a concentration peak in the near-surface layers can be observed. This peak might be attributed to impurities and/or defects that create more binding trapping sites for the D atoms, in comparison with the bulk in general.

The most noticeable outcome from these depth profiles is the clear decrease in D concentration as a result of the increase in Re content, reflected on the difference of almost one order of magnitude between the pure W sample and the W-1 at.%Re, similar to the difference between the W-1 at.%Re sample and both the W-3 and -6 at.%Re samples. However, despite the W-6 at.%Re sample shows lower concentration values than the W-3 at.%Re sample, it remains unclear whether this difference is proof of an effect arising from the increment in the Re fraction, as the ratio between these two values is of only ~ 1.15 at the damage peak.

The observations acquired form the depth profile are in agreement with the measured TDS spectra for the same set of samples, shown in Fig. 4.4. It becomes again clear that there is a significant difference in the amonut of desorbed D for different Re fractions present in the sample, being again the pure W sample the highest, followed by the W-1 at.%Re sample and then by the W-3 and -6 at.%Re samples, both with comparable spectra.

In contrast with the samples irradiated at room temperature, the TDS spectra for these samples show difference in the radiation defects' nature, according to the desorption peaks. The pure W sample shows a broad dominant peak with maximum at ~ 600 K, followed by what could be another broader but shallower peak at higher temperatures. On the other hand, the W-1 at.%Re sample shows a significant suppression of the biggest peak measured in the previous sample, making clear the presence of a second type of defects with a desorption peak at ~ 750 K.

For the W-3 and -6 at.%Re samples the first desorption peak appears to be nearly fully suppressed. The second peak is as well almost completely suppressed in the case of the W-3 at.%Re sample, however, in the case of the W-6 at.%Re it is not totally suppressed and, in fact it is shifted up to ~ 780 K.

Finally, these same analyses were performed for the samples irradiated at room temperature and annealed at high temperature. Fig. 4.5 shows the depth profiles obtained for this set of samples. Similar to the previously studied samples irradiated at high temperature, an effect produced by the Re concentration can be again observed around the damage peak. In fact, this effect shows once again an inverse relationship for three of the samples between the D concentration and the Re fraction. However, this effect is not as strong as the one observed in the previous samples, given that the maximum ratio between concentration values at damage peak is of ~ 3.5. Contrary to the regular tendency, the W-6

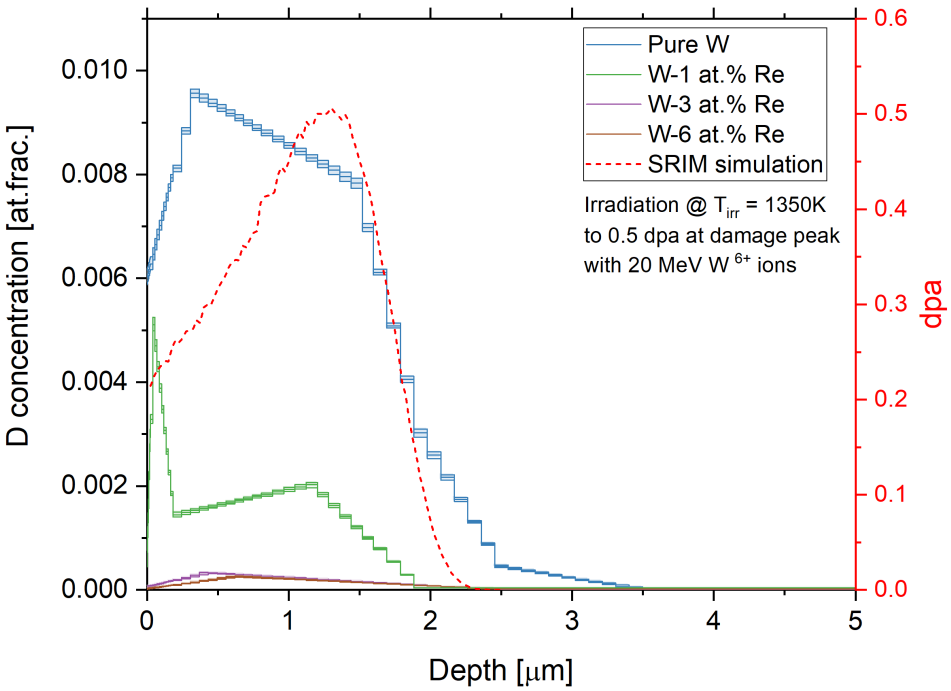

(a) Linear Scale

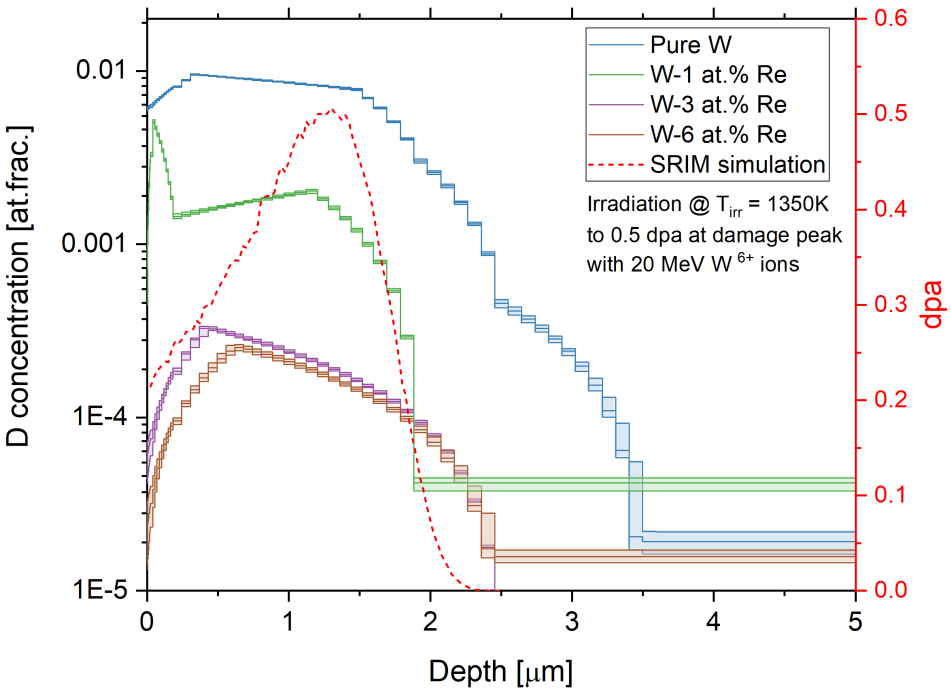

(b) Logarithmic Scale

Figure 4.3: D Depth profiles derived from NRA measurements for the set of samples irradiated at high temperature $T_{\text{irr}} = 1350$ K. SRIM calculations for the damage produced in a W sample by 20 Mev W^{6+} ions are overlayed.

at.%Re sample shows higher concentration values than the W-3 at.%Re sample, being up to 2.1 times higher in given layers.

Resembling the high T_{irr} set of samples, the pure W sample shows a higher D penetration

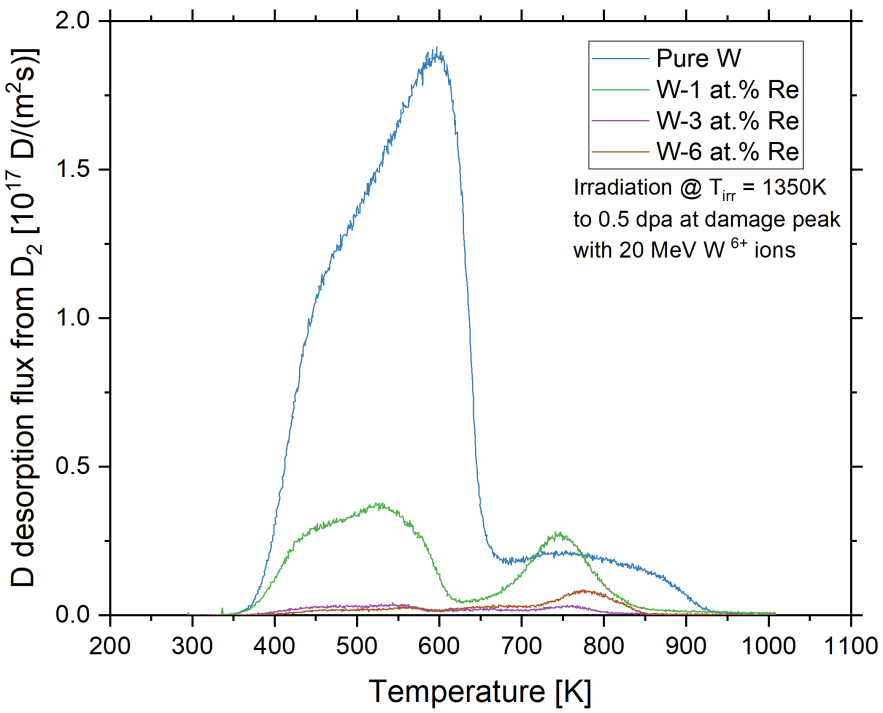

Figure 4.4: TDS spectra for the set of samples irradiated at high temperature $T_{\text{irr}} = 1350$ K, showing the D release rate of D_2 (Mass 4) molecules.

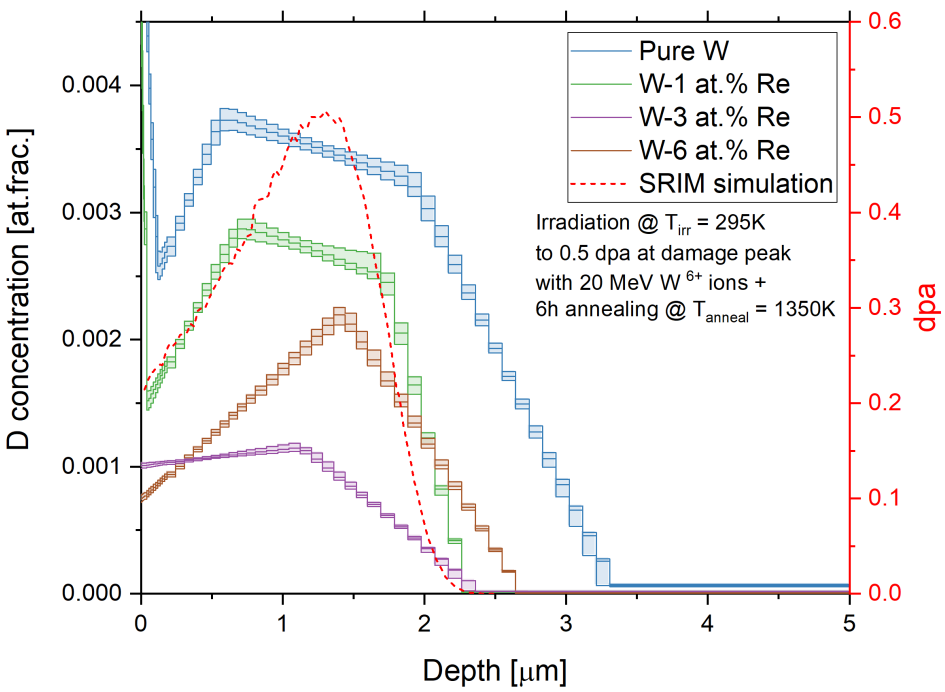

Figure 4.5: D Depth profiles derived from NRA measurements for the set of samples irradiated at room temperature $T_{\text{irr}} = 295$ K and then annealed for 6h at $T_{\text{anneal}} = 1350$ K. SRIM calculations for the damage produced in a W sample by 20 Mev W^{6+} ions are overlayed.

up until 3.3 μm deep, in contrast with the W-Re alloys where the D penetrates until around 2.5 μm. Samples like pure W and W-1 at.%Re show surface concentration peaks, suggesting once more the presence of near-surface impurities and/or defects.

Fig. 4.6 shows the measured TDS spectra for this last set of samples. The desorption fluxes enlighten higher D concentration levels for the pure W sample, and lower levels for increasing Re fractions at the alloys. Opposite to the NRA profile, the TDS spectra show higher levels of retained D for the W-3 at.%Re sample in comparison with the W-6 at.%Re sample. Additionally, the difference of these values between the 4 samples, does not seem as pronounced as in the case of the samples irradiated at high temperature, since the desorption fluxes do not reach a difference larger than an order of magnitude between any pair of samples at any temperature.

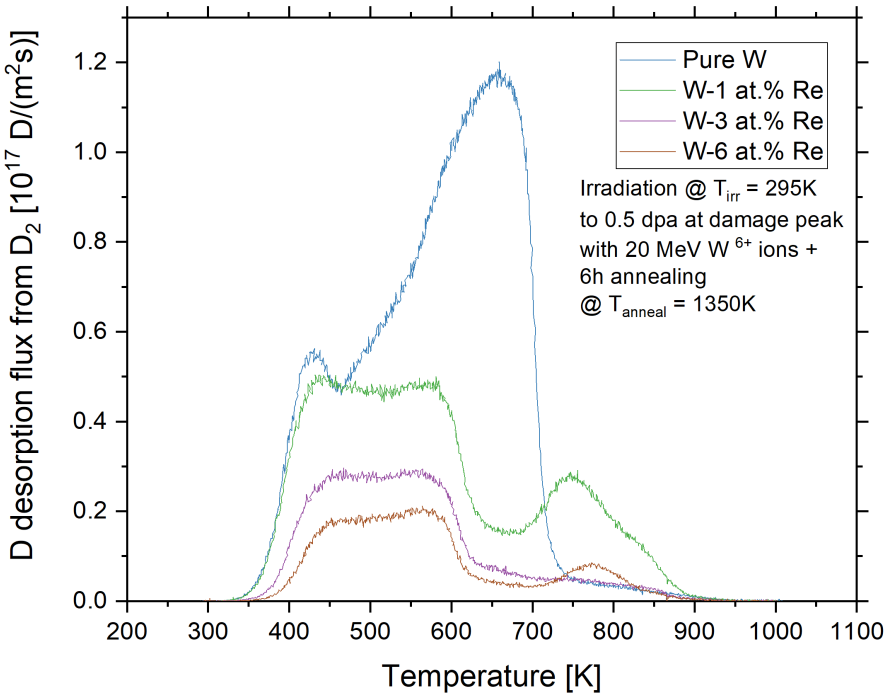

Figure 4.6: TDS spectra for the set of samples irradiated at room temperature T_{irr} = 295 K and consecutively annealed at high temperature T_{anneal} = 1350 K during 6 hours, showing the D release rate of D_2 (Mass 4) molecules.

Regarding the radiation defects, it can be observed that two peaks characterize all the spectra. In the case of the pure W sample, a broad peak with maximum at $\sim$ 650 K dominates the desorption flux, in addition to a narrower and shallower peak with maximum at $\sim$ 430 K. In the case of the W-Re alloys, this lower-temperature peak seems not only to decrease with higher Re fractions, but also it appears to broaden, creating a plateau region in the approximate range of 400-600 K for the three samples.

In the case of the desorption peak observed at $\sim$ 600 K for the pure W sample, it appears to be once more suppressed and shifted to higher temperatures in comparison with the

W-1 and -6 at.%Re samples. It can be generally observed that, compared with high T_{irr} samples, not only the desorption fluxes present a smaller reduction for higher Re fraction, but also the type of defects present in the samples seem to be different, since the general characteristics of the desorption peaks (temperature, width) seem to change substantially.

4.3 Evaluation of the rhenium fraction and temperature influence

Using both the derived depth profiles and the measured TDS spectra, it is possible to compute the total D retained in every analyzed sample, quantified as the number of atoms over a unit of surface area. This parameter can be used as one of the main quantities to assess the influence of both the rhenium fraction in the W specimens and the irradiation/annealing temperature.

In a similar fashion to previous studies, using the NRA results, it is possible to quantify the D concentration levels in the region of interest, i.e. around the damage peak. For this particular case, the average over the region ranging 0.49 - 1.79 μm depth was selected to carry out the comparison between the samples. This range was selected by dismissing the near-surface region, where impurity and defect levels might vary among samples due to undesired effects, and by focusing on the region where, roughly for most of the samples, the depth profiles show a consistent behavior, suggesting a possible maximum occupation of the available trapping sites created by the irradiation.

Fig. 4.7 shows the average D concentration values for the aforestated range for the three sets of samples. Following the analysis of the depth profiles in Sec. 4.1 and 4.2, it can be again observed that higher Re concentration levels are followed by slightly higher values of retained D for the samples damaged at room temperature and, in consequence, result detrimental for the W performance as PFM. This result would be in agreement with a recent study, which shows Kinetic Monte Carlo simulations studying the synergistic evolution of Re and irradiation effects in W-Re alloys, and concludes that, at low irradiation temperatures Re aggregates to form Re-rich clusters [48], enhancing the D retention capability, while at high temperatures Re significantly promotes the vacancy-interstitial annihilation, suppressing the D retention in the specimens. Nonetheless, it must be mentioned that, with the results obtained for these samples, this low temperature effect might not be enough to claim a reduced performance of the material, given that the average D concentration for the W-6 at.%Re sample is only $\sim$ 1.2 times higher compared with the pure W sample.

Regarding the high temperature samples, it can be first observed a clear decrease in the

D concentration compared with the previously discussed room temperature samples, with a more pronounced difference for the high T_{irr} samples. Similarly it is again observed that the Re fraction in the alloys plays a major role when evaluating the D concentration levels. For both set of samples, there is a significant decrease from the pure W sample up to the W-3 at.%Re sample, being the difference considerably more pronounced for the samples irradiated at high temperature, reaching average concentration ratios up to almost two orders of magnitude. This contrasts with the samples annealed at high temperature, whose average concentration values remain within the same order of magnitude, suggesting that there is actually a difference between the two types of treatments at high temperatures.

It remains yet unclear for the high temperature samples, whether there exists a significant effect produced when increasing the Re concentration from 3 to 6 at.%. In fact, the samples annealed at high temperature show an increase in the average D concentrated for the W-6 at.%Re, contrary to the expected tendency. This difference, as well as the decrease in the case of the samples irradiated at high temperature, might not prove a significant effect considering both the ratio between the two samples' values and the uncertainty arising from taking the average values around the peak damage.

In summary, Fig. 4.7 shows an rather small effect of the Re concentration for samples irradiated at room temperature, while showing an inverse correlation regarding the D

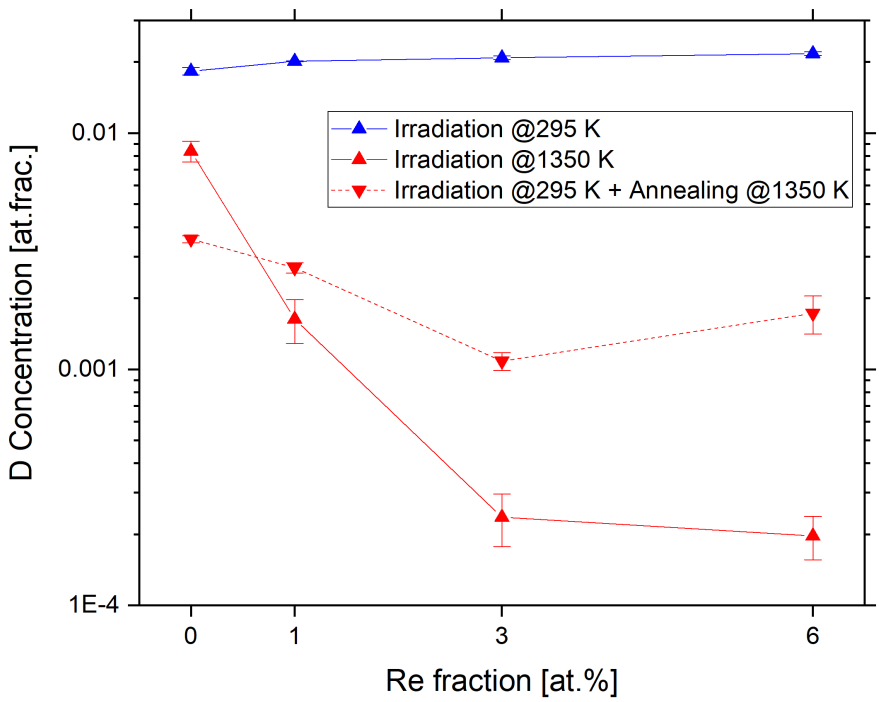

Figure 4.7: Average D concentration levels in the region surrounding the peak damage (0.49 - 1.79 μm) for all the set of samples. The temperature influences the result by up to two orders of magnitude for higher rhenium concentrations in the samples.

concentration in the case of the samples conditioned at high temperature. This last result is also in agreement with the already mentioned Monte Carlo simulation, suggesting that, for the high temperature conditions, Re actually enhances the defect suppression in the material lattice, with a more significant effect on the samples irradiated at high temperature, compared with the samples annealed at high temperature.

In addition to the D concentration levels it is possible to assess the influence of the Re fraction in the evolution of the trapping sites in the samples, through the TDS spectra already presented in Sec. 4.1 and 4.2. Fig 4.8 shows the comparison of the desorption fluxes for the case of two fixed Re fraction, considering all the results for every conditioning temperature. For this particular analysis, the TDS spectra for the undamaged set of samples were as well included in the comparison.

In the case of the pure W sample, shown in Fig. 4.8a, it is first noticeable that the undamaged sample presents desorption fluxes close to zero for all the range of temperatures. This suggests that the analyzed desorption peaks observed in the damaged samples indeed correspond to trapping sites originated due to irradiation. The temperature once again can be observed to influence the D concentration levels, reaching higher values for the samples damaged at room temperature. In fact, for the case of the high temperature samples, it appears that annealing at high temperature results in lower desorption fluxes than irradiation at high temperature. These observations are in agreement with the results obtained through the depth profiles, assessed through the average D concentration around the damage peak, exhibited in Fig. 4.7.

Furthermore, for the same case, it can also be observed that the conditioning temperature not only influences the retained D levels, but it as well changes the position and width of the desorption peaks. This indicates that for pure W, there might as well be a change in the type of the induced defects.

Fig 4.8b shows the same comparison for the W-1 at.%Re sample. Contrary to the previous case, the undamaged sample shows a shallow desorption peak with maximum at $\sim$750 K that likens to the desorption peaks present at around the same temperature for damaged samples. This peak however is neither present in the TDS spectra for the undamaged W-3 and -6 at.%Re samples (shown in Annex B), which might indicate that the type of defects characterized by this peak might be present both as radiation and intrinsic defects.

For this alloy, the temperature follows again the observed tendency, where high conditioning temperature results in lower D concentration values, being the sample damaged at high irradiation temperature the one with the lowest desorption fluxes. Regarding the defect evolution, the temperature does not seem to indicate a major change in the type of defects present in the material, as the desorption peaks don't appear to change in characteristics, only in intensity, glimpsing that the temperature only influences the defect

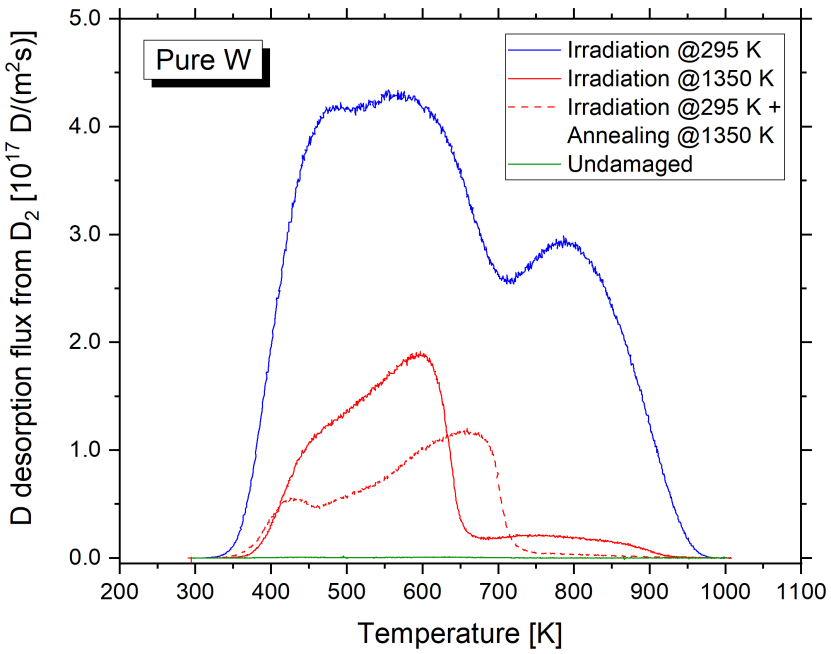

(a)

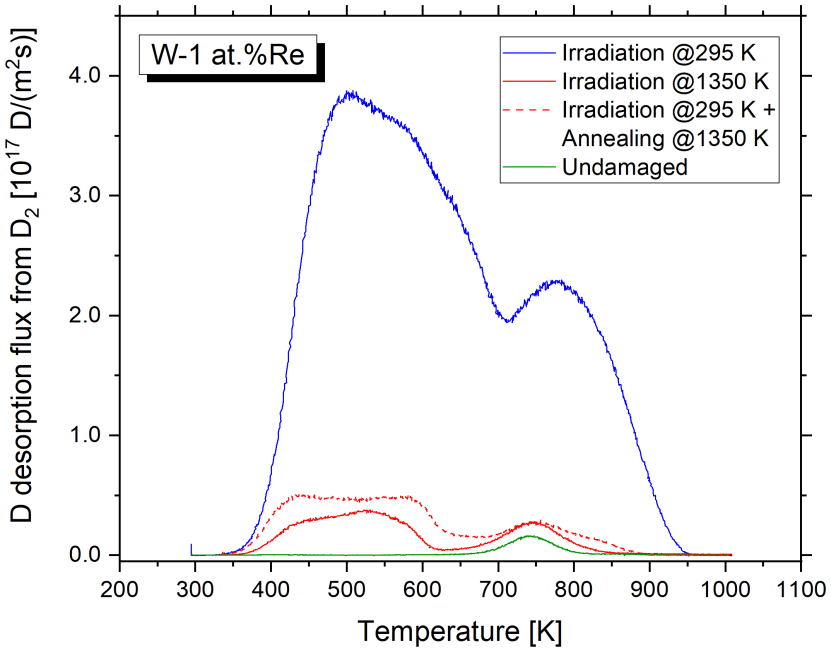

(b)

Figure 4.8: TDS spectra at different conditioning temperatures for fixed Re concentrations. a) Comparison for pure W samples, showing that the temperature influences both the defect concentration levels and the defect type evolution. No desorption fluxes for the undamaged samples indicate that peaks correspond to radiation defects; b) Comparison for W-1 at.%Re samples, showing that the temperature only influences the defect concentration levels. A desorption peak is observed for the undamaged sample, indicating that its corresponding defect type might arise from irradiation or intrinsically. Beside this point, the same characteristics were found for the other two alloys.

concentration levels. All the characteristics observed in the spectra for this Re fraction, with the exception of the peak present in the case of the undamaged sample, remain the same for the W-3 and -6 at.%Re cases.

A final assessment for the Re and temperature influence in the D trapping can be performed considering the total number of atoms retained in the samples normalized to a unit of surface area, i.e. the total D retention. Furthermore, through this parameter, it is possible to compare the results obtained from both NRA and TDS. In the case of the NRA results, the total D retained can be obtained by integrating all the D concentration values for all the calculated layers. Similarly, for the TDS results, this quantity is obtained by integrating the desorption fluxes as a function of time, considering in this case the TDS spectra of the four molecules containing D (HD, D_2, HDO, D_2O) for each sample.

Table 4.1: Total D retained in every analyzed sample normalized to a unit of surface area. The values for each sample were calculated both by integrating the concentration at every calculated layer in the depth profiles (NRA) and by integrating the desorption fluxes as a function of time, considering all molecular contributions: HD, D_2, HDO, D_2O (TDS).

	Total D retention [10^{21} D/m^2]					
	Room T_{irr}		**High T_{anneal}**		**High T_{irr}**	
	NRA	**TDS**	**NRA**	**TDS**	**NRA**	**TDS**
Pure W	3.36	3.25	0.575	0.669	1.02	0.749
W-1 at.%Re	2.92	2.43	0.325	0.391	0.204	0.227
W-3 at.%Re	3.42	2.78	0.126	0.247	0.0276	0.0517
W-6 at.%Re	3.24	2.72	0.223	0.157	0.0242	0.0676

Table 4.1 shows the values of the total D inventory, calculated both with the NRA and TDS results, for the 12 samples considered in this project. For a final time, the general tendencies found in all the previous results, concerning the Re influence in the retained D at different conditioning temperatures, can be again observed.

It can be remarked that the total D retention obtained with NRA and TDS are in a general good agreement with each other, being that in most of the cases the difference is no larger than 20%. These differences might be explained, for instance, by the sensitivity of the NRADC deconvolution results to the energy calibration of the detector or by possible effects due to single crystalline nature of the samples, e.g. ion channeling. In contrast, TDS measurements are analyzed without an intermediate data processing procedure.

Moreover, for the high T_{irr} samples, whose D retention levels are particularly low, higher contributions of the HDO molecule (mass 19) in the TDS spectra were observed, which makes the accurate quantification more challenging.

Bigger discrepancies, like the case of the W-3 and -6 at.% samples, both irradiated at high temperature (factor ∼2 and ∼3, respectively), might as well be attributed to laterally non-uniform damaging of the samples. Given that the NRA results assume uniform damage in all the sample surface, by taking the measurement point (selected to be the center) as a reliable representation of the whole surface, this lateral inhomogeneities might explain the big discepancies with the TDS results, as TDS measures all the D atoms desorbed from any point in the surface, regardless of the damage level distribution.

These inhomogenities can be revealed through the lateral scanning technique explained in Sec. 3.2.1. Fig. 4.9 shows the proton counts normalized to the maximum value measured with the *ProL* detector (selected for higher statistics) at different relative positions to the center of each sample. The mentioned W-3 and -6 at.% samples appear to have non uniform proton counts, reaching values at given positions of only 80% with respect to the maximum in both cases. This might be the explanation of the big differences in the total D obtained for these samples, comparing the NRA with the TDS results.

Additionally, Fig. 4.9 shows the same lateral scanning for another selected sample, W-3 at.%Re irradiated at room temperature. In this case, a nearly perfectly-uniform distribution of the proton counts, which agrees with the fact that the difference of the total D

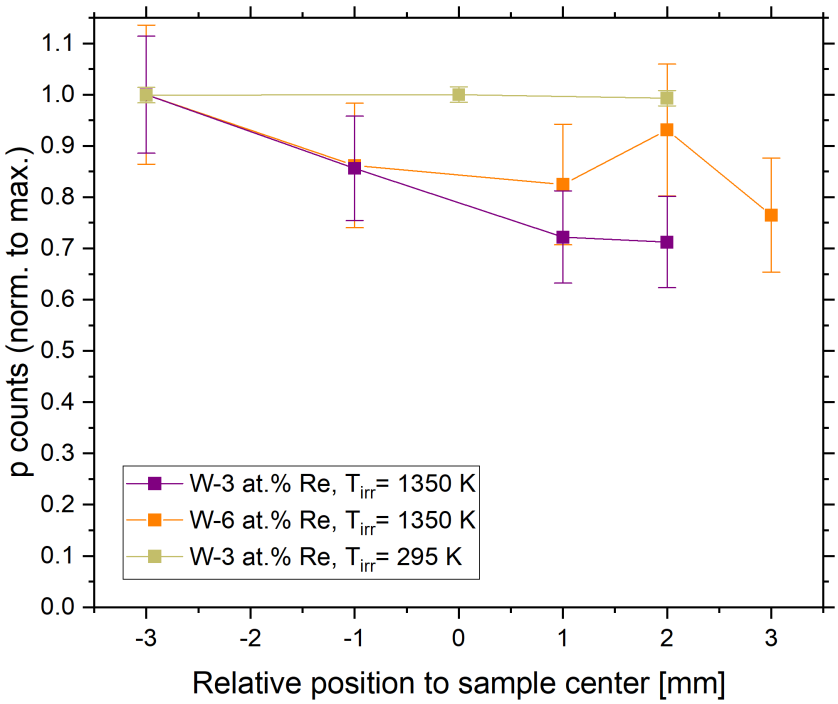

Figure 4.9: Lateral scanning obtained with the proton counts measured with the *ProL* detector. Non-uniform radiation damage levels are appreciated for the W-3 and -6 at.% samples, damaged at high temperature, can be observed. Uniform damage was measured for the W-3 at.%Re sample irradiated at room temperature. The inhomogenities in the radiation damage on the surface might explain some discrepancies between NRA and TDS results.

retention values obtained by TDS and NRA differ by only ∼20%. Even though the inhomogenieties in the damage don't explain all the discrepancies between TDS and NRA, it indeed indicates that these minor inconsistencies might be attributed to the imperfections of the experimental techniques, rather than to a misinterpretation of the obtained results.

Chapter 5

Conclusions and Outlook

The objective of this thesis is to carry on with the line of research studying the rhenium influence on the performance of tungsten as PFM. Following previous results, a systematic comparison taking into account some of the known relevant variables was performed. Sets of single crystal W samples with different Re concentrations (0, 1, 3 and 6 at.%), were damaged with 20 MeV W^{6+} up to 0.5 dpa at damage peak at room temperature $T_{\mathrm{irr}} = 295$ K, and high temperature $T_{\mathrm{irr}} = 1350$ K. One set of samples damaged at room temperature was additionally annealed at $T_{\mathrm{anneal}} = 1350$ K. All samples were subsequently exposed to D plasma in an ECR source at a sample temperature of 370 K for 72h. The D retention in all the samples was determined through the analysis of the D depth profiles and D desorption flux spectra, measured with Nuclear Reaction Analysis (NRA) and Thermal Desorption Spectroscopy (TDS), respectively.

The main results obtained from this work can be summarized in 3 main points:

1. The Re concentration in the alloys seem to have a strong influence for the case of the samples conditioned at high temperature, with the D concentration values dropping for higher Re fractions. This effect is specially evident for the samples irradiated at high temperature, being the D concentration for the highest Re fraction almost two orders of magnitude lower than the case of the pure W sample. This result agrees with theoretical simulations performed in other studies, claiming that the Re presence enhances the vacancy-interstitial annihilation, i.e. suppresses defects where D might be trapped. These same simulations claim that Re might be detrimental for low irradiation temperature, by forming clusters that facilitate the D retention. This effect, however, was not observed to a significant level, since for room temperature samples the D retention increased only slightly for higher Re fractions.

2. The temperature at which the samples are conditioned enhances the suppression of the D trapping sites, effect that becomes more pronounced for higher Re con-

centrations. For fixed Re fractions, it was observed that the retained D values for room and high temperature differed between each other by one or even two orders of magnitude. For the W-Re samples, it was shown that the temperature influences mainly the defect concentration, with only little influence on the evolution of the nature of the trapping sites created by irradiation.

3. Based on the observed D concentration levels, there is a difference between high temperature damaging and room temperature damaging followed by high temperature annealing, being the first case the one showing lower trapped D and stronger influence from the Re concentration in the sample. This might be an indication that the defect evolution mechanisms differ due to irradiation in reactor-like conditions, rather than remaining comparable to simple exposure of the sample to high temperatures.

It is important to note that these general conclusions were reached independently through the two experimental techniques applied in this work, NRA and TDS. This general good agreement between both analysis reinforces the validity of the results. Furthermore, it is worth remembering that all these observations were already done independently by the studies preceding this thesis. Through the cross-validation of the previously observed effects, taking simultaneously into account several variables, it has been once more demonstrated that, in a fusion reactor environment, Re will indeed influence the performance of tungsten-based PFC.

For the reactor conditions raised in this study, Re, originating as a W transmutation element due to the fast fusion neutrons, seem to have a beneficial effect regarding the concentration of radiation defects produced by the byproducts of the DD and DT reactions. This synergistic influence must be nonetheless further investigated. Future work can be performed by continuing to assess whether the Re presence in the W specimens keeps showing an influence at concentrations higher than the ones studied in this work, inasmuch as the results obtained did not show a clear difference between the W-3 and -6 at.%Re samples. Similarly, the cross-validation performed can as well be extended to other previously studied parameteres, considering, for instance, different damaging levels, i.e. higher and lower dpa, or other sample temperatures during irradiation.

The understanding of Re as a transmutation element has so far proven to be key for the assessment of W as a candidate material for the PFCs. If the presence of this element keeps to be proven advantageous for the material's performance, W might indeed become closer to become the chosen PFM for many of the PFCs for future reactor designs. Although this synergy will only be fully assessed directly during ITER's first years of operations, the surrogate techniques applied in this thesis and precedent works result relevant to understand tungsten's potential as PFM and, in consequence, bring us closer to find the

reactor's wall conditions needed to operate an efficient and functioning fusion device.

Bibliography

[1] R. Toschi. Nuclear fusion, an energy source. *Fusion Engineering and Design*, 36(1): 1–8, 1997.

[2] F. Chen. *Introduction to plasma physics and controlled fusion*, volume 1, chapter Plasma Applications, pages 356–385. Springer, 2016.

[3] J. Linke et al. Challenges for plasma-facing components in nuclear fusion. *Matter and Radiation at Extremes*, 4(5), 2019.

[4] J. Roth et al. Recent analysis of key plasma wall interactions issues for ITER. *Journal of Nuclear Materials*, 390:1–9, 2009.

[5] G. Federici et al. Plasma-material interactions in current tokamaks and their implications for next step fusion reactors. *Nuclear Fusion*, 41(12):1967, 2001.

[6] Y. Ueda et al. Baseline high heat flux and plasma facing materials for fusion. *Nuclear Fusion*, 57(9):092006, 2017.

[7] G. Pintsuk. Tungsten as a plasma-facing material. In *Comprehensive Nuclear Materials*, volume 4, pages 551–581. Elsevier, 2012.

[8] M.R. Gilbert and J-Ch. Sublet. Neutron-induced transmutation effects in W and W-alloys in a fusion environment. *Nuclear Fusion*, 51(4):043005, 2011.

[9] B. Tyburska-Püschel and V. Kh. Alimov. On the reduction of deuterium retention in damaged Re-doped W. *Nuclear Fusion*, 53(12):123021, 2013.

[10] Y. Hatano et al. Deuterium retention in W and W-Re alloy irradiated with high energy Fe and W ions: Effects of irradiation temperature. *Nuclear Materials and Energy*, 9:93–97, 2016.

[11] J. Wang et al. Deuterium retention in W and binary W alloys irradiated with high energy Fe ions. *Journal of Nuclear Materials*, 545:152749, 2021.

[12] M.A. Pick and K. Sonnenberg. A model for atomic hydrogen-metal interactions - Application to recycling, recombination and permeation. *Journal of Nuclear Materials*, 131(2-3):208–220, 1985.

[13] M. Zibrov. *The influence of radiation, mechanical, and plasma-induced damage on deuterium retention in tungsten.* PhD thesis, Technische Universität München, 2018.

[14] J. Lennard-Jones. Processes of adsorption and diffusion on solid surfaces. *Transactions of the Faraday Society*, 28:333–359, 1932.

[15] W. Möller and J. Roth. Implantation, Retention and Release of Hydrogen Isotopes in Solids. In *Physics of Plasma-Wall Interactions in Controlled Fusion*, pages 439–494. Springer Science & Business Media, 2013.

[16] G.S. Was. *Fundamentals of radiation materials science: metals and alloys*, chapter The displacement of atoms, pages 73–124. Springer, 2016.

[17] J.A. Mascitti et al. Method for the Calculation of DPA in the Reactor Pressure Vessel of Atucha II. *Science and Technology of Nuclear Installations*, 2011, 2011.

[18] M.J. Norgett, M.T. Robinson, and I.M. Torrens. A proposed method of calculating displacement dose rates. *Nuclear Engineering and Design*, 33(1):50–54, 1975.

[19] J. Ziegler. Srim 2013. `http://www.srim.org/`.

[20] G. Federici et al. Effects of ELMs and disruptions on ITER divertor armour materials. *Journal of Nuclear Materials*, 337:684–690, 2005.

[21] R.A. Pitts et al. Physics basis and design of the ITER plasma-facing components. *Journal of Nuclear Materials*, 415(1):S957–S964, 2011.

[22] Y. Ueda et al. Research status and issues of tungsten plasma facing materials for ITER and beyond. *Fusion Engineering and Design*, 89(7-8):901–906, 2014.

[23] Z Wang et al. Effect of rhenium on defects evolution behavior in tungsten under irradiation. *Nuclear Fusion*, 61(3):036037, 2021.

[24] N.P. Bobyr et al. Preparation of macrocrystalline tungsten-based alloys by electron-beam floating zone melting. *Inorganic Materials*, 57(12):1307–1316, 2021.

[25] R. Butz et al. Preparation of stepped tungsten single crystal surfaces. *Physica Status Solidi (a)*, 27(1):205–212, 1975.

[26] W.D. Callister Jr. *Materials Science and Engineering An Introduction*, chapter Application and processing of metal alloys. Wiley, 2018.

[27] Max Planck Institute for Plasma Physics. Tandem accelerator. `https://www.ipp.mpg.de/4218067/beschleuniger`.

[28] T. Schwarz-Selinger. Deuterium retention in MeV self-implanted tungsten: Influence of damaging dose rate. *Nuclear Materials and Energy*, 12:683–688, 2017.

[29] G.S. Was and S.J. Zinkle. Toward the use of ion irradiation to predict reactor irradiation effects. In *Comprehensive Nuclear Materials*, volume 1, pages 468–484. Elsevier, 2020.

[30] E. Getto et al. Effect of irradiation mode on the microstructure of self-ion irradiated ferritic-martensitic alloys. *Journal of Nuclear Materials*, 465:116–126, 2015.

[31] J.G. Gigax et al. The influence of ion beam rastering on the swelling of self-ion irradiated pure iron at 450 C. *Journal of Nuclear Materials*, 465:343–348, 2015.

[32] R.E. Stoller et al. On the use of SRIM for computing radiation damage exposure. *Nuclear Instruments and Methods in Physics Research Section B: Beam Interactions with Materials and Atoms*, 310:75–80, 2013.

[33] K. Nordlund et al. Primary Radiation Damage in Materials. Review of Current Understanding and Proposed New Standard Displacement Damage Model to Incorporate in Cascade Defect Production Efficiency and Mixing Effects. Technical report, Organisation for Economic Co-Operation and Development, 2015.

[34] T. Schwarz-Selinger. Unpublished.

[35] A. Manhard, T. Schwarz-Selinger, and W. Jacob. Quantification of the deuterium ion fluxes from a plasma source. *Plasma Sources Science and Technology*, 20(1):015010, 2011.

[36] A. Manhard, M. Balden, and U. Von Toussaint. Blister formation on rough and technical tungsten surfaces exposed to deuterium plasma. *Nuclear Fusion*, 57(12): 126012, 2017.

[37] L. Gao et al. Deuterium supersaturation in low-energy plasma-loaded tungsten surfaces. *Nuclear Fusion*, 57(1):016026, 2016.

[38] M. Nastasi, J. Mayer, and Y. Wang. *Ion Beam Analysis: Fundamentals and Applications*, chapter Nuclear reaction analysis, pages 113–140. CRC Press, 2014.

[39] B. Wielunska et al. Cross section data for the D(3He,p)4He nuclear reaction from 0.25 to 6 MeV. *Nuclear Instruments and Methods in Physics Research Section B: Beam Interactions with Materials and Atoms*, 371:41–45, 2016.

[40] M. Mayer et al. Quantitative depth profiling of deuterium up to very large depths. *Nuclear Instruments and Methods in Physics Research Section B: Beam Interactions with Materials and Atoms*, 267(3):506–512, 2009.

[41] A. Manhard. *Deuterium Inventory in Tungsten After Plasma Exposure: A Microstructural Survey.* PhD thesis, Universität Augsburg, 2013.

[42] M. Mayer. SIMNRA User's Guide. Technical report, 1997, Max Planck Institute for Plasma Physics.

[43] K. Schmid and U. Von Toussaint. Statistically sound evaluation of trace element depth profiles by ion beam analysis. *Nuclear Instruments and Methods in Physics Research Section B: Beam Interactions with Materials and Atoms*, 281:64–71, 2012.

[44] A. Van Gorkum and E. Kornelsen. Quantitative thermal desorption spectrometry of ionically implanted inert gases - I. Fundamental aspects. *Vacuum*, 31(2):89–98, 1981.

[45] E. Kornelsen and A. Van Gorkum. Quantitative thermal desorption spectrometry of ionically implanted inert gases - II. Technical requirements. *Vacuum*, 31(2):99–111, 1981.

[46] E. Salançon et al. Redeposition of amorphous hydrogenated carbon films during thermal decomposition. *Journal of Nuclear Materials*, 376(2):160–168, 2008.

[47] E. Tomkova. TDS spectra analysis. *Surface science*, 351(1-3):309–318, 1996.

[48] Y. Li et al. Temperature-dependent synergistic evolution mechanism of rhenium and irradiation defects in tungsten-rhenium alloys. *Journal of Materials Science & Technology*, 145:221–234, 2023.

[49] S.P. Kumar, D. Balaji, and T.R. Mandlimath. Characterization of flexible ceramics. In *Advanced Flexible Ceramics*, pages 25–43. Elsevier, 2023.

Appendix

A EDX analysis

Energy Dispersive X-Ray (EDX) analysis is an experimental technique that aims to quantify the chemical composition in samples, by analyzing the X-rays emitted by the specimen when it is hit with high-energy electromagnetic radiation. When the incident beam hits an atom present in the sample, which contains unexcited electrons in discrete energy levels that are characteristic of an element, an ionization process takes place, creating an electron hole in the atom. With the aid of a strong electric field, the electrons and holes are attracted to opposite ends of the detector, thus generating current pulses whose intensity is proportional to the number of electron-hole pairs created. With this information, a energy spectra characterizing the amount of given elements in the sample can be acquired [49].

EDX studies were performed for this project as an attempt to verify the Re guaranteed by the manufacturer in the used samples. Four samples, each containing a different Re concentration, were studied using this technique. The acquired EDX spectra acquired for the near-surface region of the samples is shown in Fig. A.1 and the total atomic percentage contributions calculated through these spectra are described in Table A.1.

Table A.1: Atomic percentage calculated with EDX analysis for one W sample for each of the studied Re concentration.

	W	Re	C	O	Ni
Pure W	39.6 ± 0.2 %	-	59.4 ± 0.3 %	0.5 ± 0.1 %	0.5 ± 0.1 %
W-1 at.%Re	39.1 ± 0.2 %	0.5 ± 0.1 %	59.7 ± 0.3 %	0.1 ± 0.1 %	0.5 ± 0.1 %
W-3 at.%Re	39.2 ± 0.2 %	0.6 ± 0.1 %	59.6 ± 0.3 %	-	0.5 ± 0.0 %
W-6 at.%Re	37.8 ± 0.2 %	1.4 ± 0.1 %	59.7 ± 0.3 %	0.7 ± 0.1 %	0.4 ± 0.0 %

From the obtained results it can be first noted that Re is actually present in the expected samples. However, large contributions from contaminating elements in the near-surface

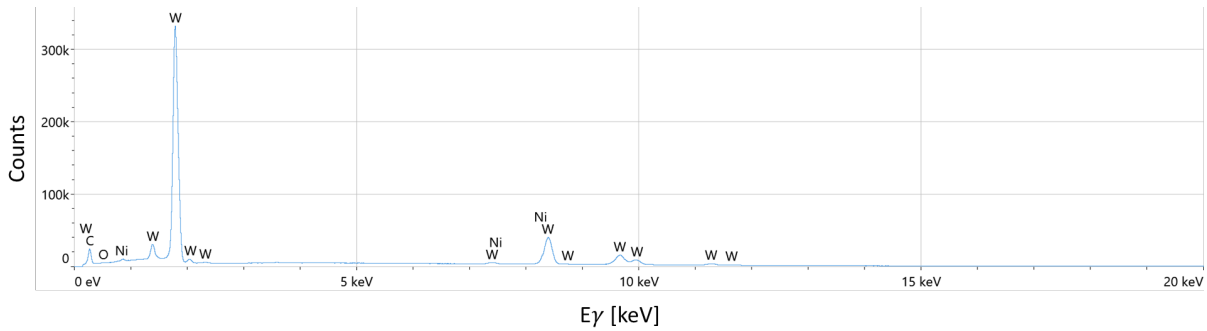

(a) Pure W

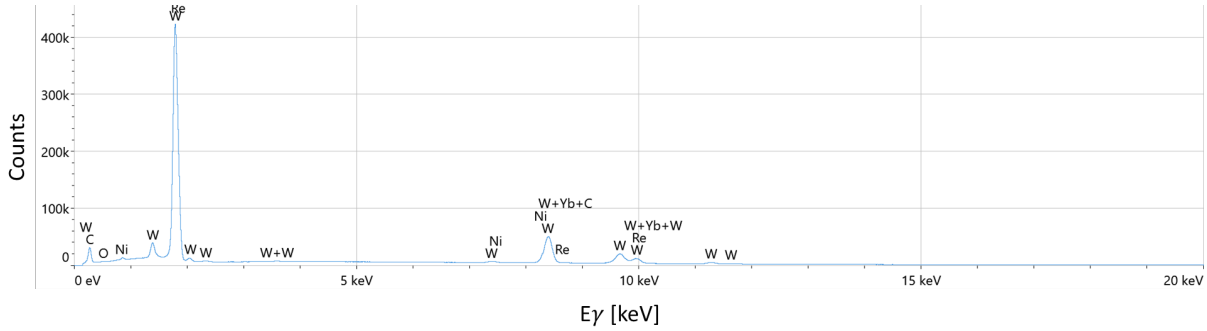

(b) W-1 at.%Re

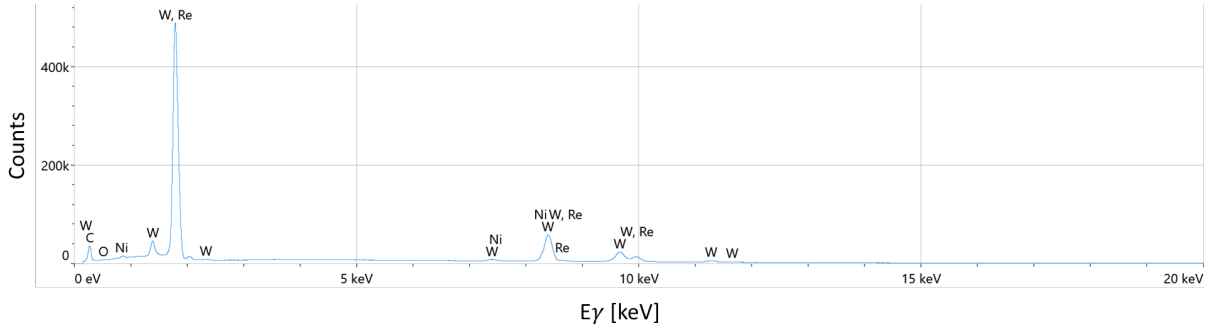

(c) W-3 at.%Re

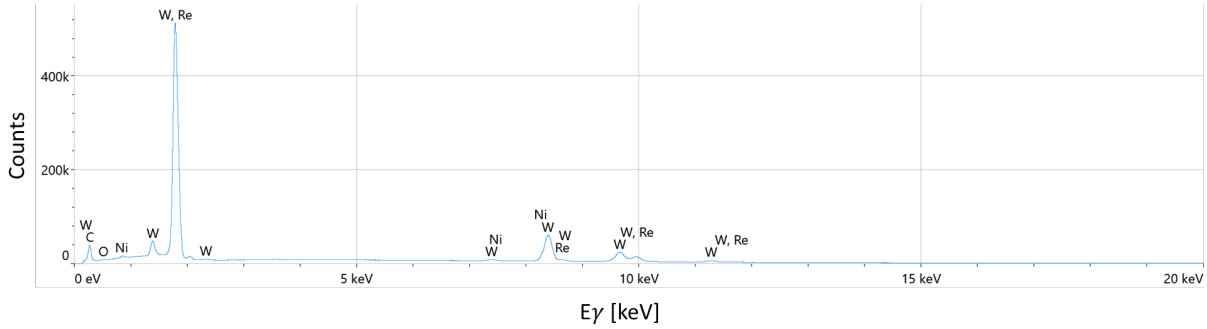

(d) W-6 at.%Re

Figure A.1: EDX analysis performed for one W sample for each of the studied Re concentration. Beside W and Re, several elements in the form of contamination were present, mainly C, O, and Ni.

region can as well be observed, being carbon the largest of them. This undesired contributions obscure the real proportion between W and Re that should characterize the

whole bulk. Although it can be observed that the Re presence increases for each sample, as it is expected, the real Re concentration cannot be determined with this analysis. It is worth mentioning that a normalization taking into account only the Re and W contributions would not be accurate given the non-linear response of the material given different chemical contributions.

B TDS spectra for fixed Re fractions (continuation)

Following the results presented in Sec. 4.3, the TDS spectra comparison for the W samples containing 3 and 6 at.%Re concentrations are shown in Fig. B.1 and Fig. B.2, respectively. As it was aforementioned in the discussion, these alloys present a similar behavior to the W-1 at.%Re samples when varying the temperature at which they were conditioned: for higher temperatures, the desorption fluxes are reduced, indicating a suppression of defects created by irradiation. The temperature does not seem to influence the type of defects present in the specimens. In contrast to the 1 at.%Re alloy, the undamaged samples don't present any desorption peak. The TDS spectra are as well presented with logarithmic scale to emphasize the difference between desorption fluxes.

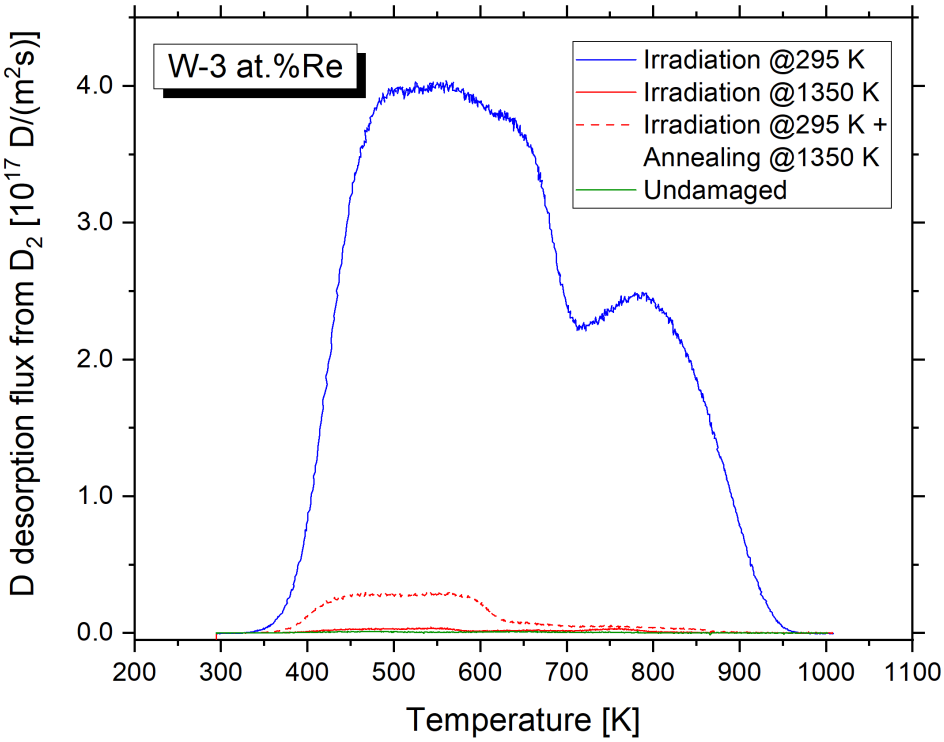

(a) Linear Scale

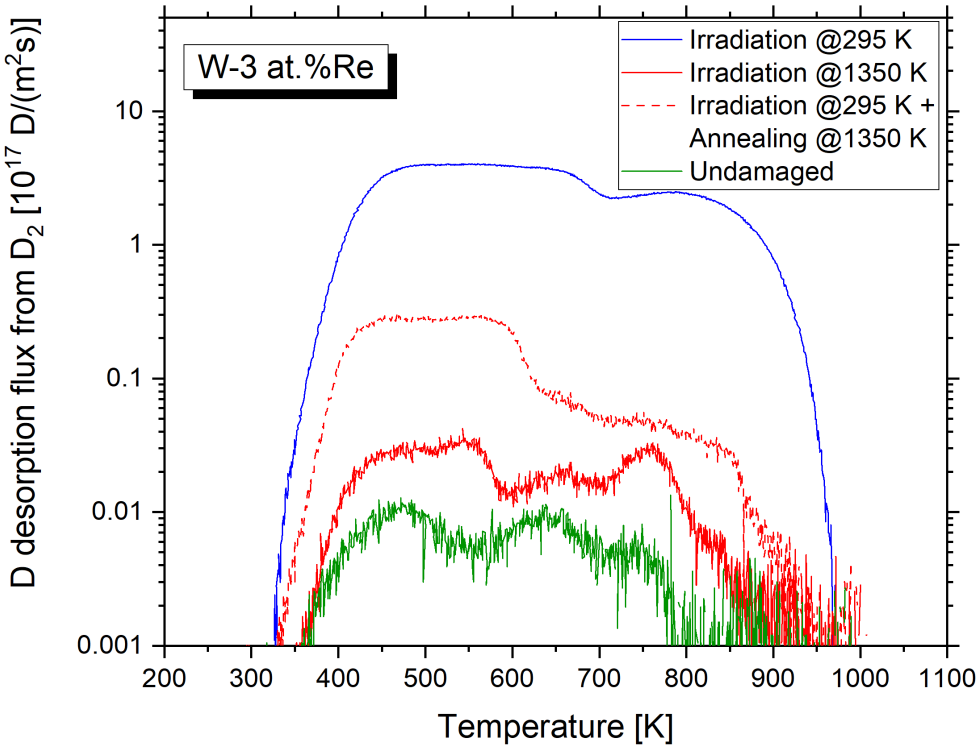

(b) Logarithmic Scale

Figure B.1: TDS spectra comparison for W-3 at.%Re samples, showing the temperature influence in the defect concentration levels.

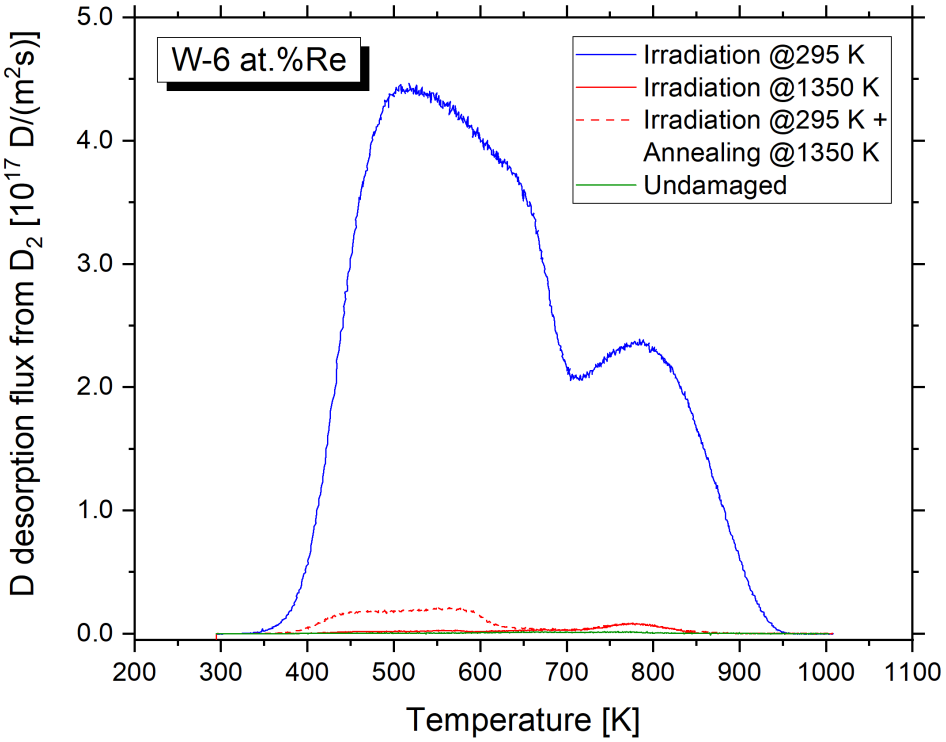

(a) Linear Scale

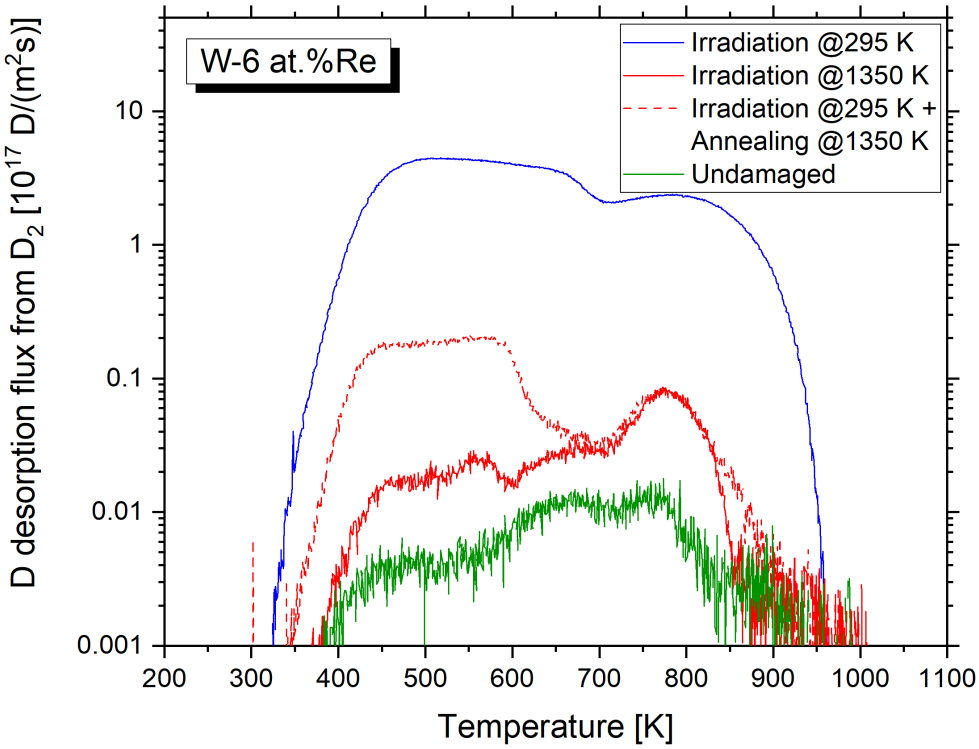

(b) Logarithmic Scale

Figure B.2: TDS spectra comparison for W-6 at.%Re samples, showing the temperature influence in the defect concentration levels.